International Journal of Mechanical Sciences 325 (2026) 111841

Contents lists available at ScienceDirect

International Journal of Mechanical Sciences

journal homepage: www.elsevier.com/locate/ijmecsci

Surface-tension-driven dynamic buckling and multimodal oscillations of inhomogeneous rod loops

Yaxin Fang, Chengyao Zhang, Xiying Li, Yi Man, Xin Yi *

School of Mechanics and Engineering Science, Peking University, Beijing 100871, China

ARTICLE INFO

Keywords:
Nonlinear dynamics
Structural instability
Elastocapillarity
Lobe coalescence
Lobe collapse
Interfacial dissipation

ABSTRACT

While buckling of elastic loops is well understood in the static regime, its dynamic counterpart under sudden loading can exhibit oscillatory and multimodal deformations and remains comparatively less explored, particularly in the presence of material inhomogeneity and viscous interfacial dissipation. Here, we combine theoretical and experimental analyses to investigate surface-tension-driven elastic rod loops in soap films, where rupture of either the surrounding film or the film enclosed by the loop imposes sudden loading, and examine how material inhomogeneity and soap-film dissipation shape the resulting buckling and oscillatory dynamics. For homogeneous loops, we identify the transition from low-tension periodic oscillations to high-tension multimodal buckling and reveal nonlinear phenomena including mode coupling and mode-number reduction at high surface tension. We further examine how material inhomogeneity reshapes the instability landscape. Stiffness inhomogeneity sharpens spatial localization of bending and lowers stability thresholds, while density contrast induces temporal desynchronization and complex multi-frequency oscillations. Soap-film dissipation suppresses the oscillation amplitude and frequency and accelerates relaxation. Across all cases considered, mode-number reduction proceeds through two pathways: lobe coalescence and lobe collapse. These insights highlight the sensitivity of closed slender structures to coupled elastic, inertial, and interfacial viscosity effects, and suggest principles for designing filamentary systems whose dynamic morphologies can be tuned through targeted material patterning or interface engineering.

1. Introduction

Buckling instabilities driven by pressure differences or distributed loads are ubiquitous in engineering, biological, and soft-matter systems. Vertical oil and fuel storage tanks under strong winds and deep-sea pipelines under high hydrostatic pressure may induce structural collapse, with geometric imperfections or material degradation significantly amplifying failure risk [1,2]. Analogous pressure-driven deformations arise in biological structures such as arterial vessels and cardiac valves, where pulsatile flow and active muscular contraction may trigger periodic buckling accompanied by multimodal shape changes [3–6]. Beyond failure scenarios, pressure-induced deformation and buckling can also be harnessed constructively [7,8]: recent studies have demonstrated that fluidic or pneumatic actuation can enable controlled shape transformation in soft robotic and endovascular devices [9–13].

From a mechanistic standpoint, buckling of closed elastic rings or loops may be broadly classified into static and dynamic instabilities, depending on the loading protocol and the role of inertia. In static or quasi-static buckling, loading is applied sufficiently slowly that inertial effects are negligible [14–16]. Instability is identified through the loss of equilibrium or bifurcation of stationary solutions, and post-buckling configurations are governed by elastic energy minimization. Classical studies of elastic ring buckling have predominantly focused on this regime.

Within the elastica framework, circular rings or arches under uniform or directional pressure have been systematically analyzed, yielding well-established critical conditions and mode structures [17–24]. These analyses have been extended to position-dependent loading [3,25], area constraints [26], the Euler–Plateau and Kirchhoff–Plateau problems, which consider elastic loops spanned by soap films with and without torsional effects, respectively [27–31], as well as related formulations involving elastic boundaries coupled to curvature-elastic membranes, such as the Euler–Helfrich problem [32,33]. They have also been extended to account for self-contact, revealing transitions from point contact to finite-length contact in the post-buckling regime [3,34]. More recently, the role of external confinement, either rigid or deformable, has been shown to fundamentally alter admissible deformation modes and stability thresholds [35–44]. Such confinement-induced buckling phenomena are of particular relevance in flexible and

* Corresponding author.
E-mail address: xyi@pku.edu.cn (X. Yi).

https://doi.org/10.1016/j.ijmecsci.2026.111841
Received 15 December 2025; Received in revised form 11 June 2026; Accepted 14 June 2026
Available online 17 June 2026

stretchable electronics, where controlled deformations enable mechanical compliance and conformal integration with tissues [45–47].

When loading is applied dynamically, however, inertia and time-dependent effects fundamentally alter the system response. In this regime, elastic rings may transiently access configurations far from static equilibria, excite multiple competing deformation modes, and undergo oscillatory or multimodal responses involving mode interaction and coalescence. As a result, neither the critical conditions nor the dominant deformation patterns can be inferred from static stability analysis alone. Instead, the system behavior depends on a combination of elastic properties, mass distribution, loading protocol, and dissipation mechanisms.

Theoretical contributions in this direction include studies of vibrations of circular rings and arches [48–51], as well as dynamic buckling under impulsive or rapidly applied loads [52–58]. More recently, experiments on elastic rings coupled to soap films have shown that sudden removal of surface tension can excite high-order buckling modes that are inaccessible under static conditions, with pattern selection governed by mode growth and transient dynamics [59,60]. Related non-equilibrium phenomena have also been reported in soap-film systems subject to continuous boundary deformation, where abrupt topological transitions occur through boundary singularities at critical stages of deformation [61], phenomena that lie beyond the scope of static minimal-surface theory [27,28]. Dynamic buckling has also been observed in other filament–fluid systems. For example, hydrodynamic compression of a bacterial flagellar hook can trigger a buckling instability that enables rapid reorientation during swimming [62]; at larger scales, droplet impact on a cantilevered filament can generate transient compressive stress waves and excite buckling modes [63].

Despite these advances, three important aspects of ring–film dynamics remain insufficiently understood. First, the mechanisms underlying mode-number reduction during post-buckling evolution remain unclear, including the pathways through which higher-order modes transition to lower-order configurations. Second, the role of material inhomogeneity, such as spatial variations in bending stiffness or mass density, has received little attention in the context of dynamic buckling and post-instability evolution, despite the prevalence of such heterogeneities in engineered and biological filamentary structures and their demonstrated influence on deformation localization during the flow-induced buckling of non-uniform microfilaments [64,65]. Third, the influence of viscous dissipation associated with the soap film has not been quantitatively incorporated into most dynamic models, although it controls oscillation amplitude, frequency, and relaxation dynamics and may effectively represent time- or space-dependent loading conditions arising from fluid–structure interactions.

In this work, we investigate the dynamic buckling and oscillatory response of surface-tension-driven elastic rod loops in soap films through a combined theoretical and experimental approach. The system is driven out of equilibrium by film rupture: rupture of either the surrounding film or the film enclosed by the loop imposes a sudden loading, while viscous dissipation in the film attenuates the ensuing rod motion. We focus on how material heterogeneity and interfacial dissipation influence the instability and its subsequent evolution.

The remainder of this paper is organized as follows. Section 2 presents the theoretical model, including the governing equations, boundary and initial conditions, and the power-balance relation. Section 3 describes the experimental setup and methods. Section 4 analyzes the dynamic response of homogeneous rod loops, including low-pressure periodic oscillations, high-pressure multimodal buckling, the effects of soap-film dissipation, and the emergence of lobe-number reduction through nonlinear lobe collapse and lobe coalescence. Section 5 extends the analysis to inhomogeneous rod loops and examines how stiffness contrast, density contrast, and their combined effects influence transient dynamics, mode selection, nonlinear interactions, energy transfer, and the associated lobe-number reduction mechanisms. Finally, Section 6 summarizes the main findings and discusses their implications.

2. Theoretical modeling

This section develops a theoretical model for the surface-tension-driven dynamics of an elastic rod loop in a soap film. Following rupture of either the outer film or the film enclosed by the loop, surface tension imposes a sudden loading that drives the system out of equilibrium. We formulate the governing equations for the planar rod loop dynamics (Section 2.1), specify the boundary and initial conditions (Section 2.2), and derive a power-balance relation characterizing the interplay among bending energy, surface energy, kinetic energy, and viscous dissipation (Section 2.3).

2.1. Governing equations

The loop is modeled as an inextensible, unshearable closed thin elastic rod of circular cross-section, constrained to undergo in-plane deformation. This assumption excludes out-of-plane bending and twist–bend coupling, which may become energetically favorable for sufficiently long or compliant filaments, at higher surface tension, or in the presence of pre-twist [27,28]. Here, we restrict attention to the planar deformations observed in our experiments. The rod configuration is described using a Cartesian coordinate system (x, y). The rod centerline is represented by a planar curve $\mathbf{r}(s,t) = x(s,t)\mathbf{e}_x + y(s,t)\mathbf{e}_y$, parameterized by arclength s and time t, where $\mathbf{e}_x$ and $\mathbf{e}_y$ are unit vectors along the Cartesian x- and y-axes, respectively. Along the rod, a local orthonormal frame $\{\mathbf{t}, \mathbf{n}\}$ is introduced, where the unit tangent vector $\mathbf{t}(= \mathrm{d}\mathbf{r}/\mathrm{d}s)$ and the unit normal vector $\mathbf{n}$ satisfy $\mathrm{d}\mathbf{t}/\mathrm{d}s = \kappa\mathbf{n}$ and $\mathrm{d}\mathbf{n}/\mathrm{d}s = -\kappa\mathbf{t}$, with κ denoting the curvature. Defining $\theta(s,t)$ as the angle between the x-axis and the tangent vector $\mathbf{t}$ gives $\mathbf{t} = \cos\theta\mathbf{e}_x + \sin\theta\mathbf{e}_y$, $\mathbf{n} = -\sin\theta\mathbf{e}_x + \cos\theta\mathbf{e}_y$, and $\kappa = \mathrm{d}\theta/\mathrm{d}s$. As illustrated in Fig. 1, the normal vector $\mathbf{n}$ is directed toward the interior of the rod loop.

The rod has length L, mass density $\rho(s)$, Young's modulus $E(s)$, and cross-sectional area A, moment of inertia I, and bending stiffness $B(s) = E(s)I$.

The rod dynamics follow the balances of linear and angular momentum as functions of arclength s and time t [60,66]

$$\frac{\partial \mathbf{F}}{\partial s} + p\mathbf{n} + \mathbf{f}_\mathrm{h} = \rho A \frac{\partial^2 \mathbf{r}}{\partial t^2} \quad \text{and} \quad \frac{\partial \mathbf{M}}{\partial s} + \mathbf{t} \times \mathbf{F} = \rho I \mathbf{n} \times \frac{\partial^2 \mathbf{n}}{\partial t^2}, \tag{1}$$

where $\mathbf{F}$ and $\mathbf{M}(= B\kappa\, \mathbf{t} \times \mathbf{n})$ denote the internal force and moment resultants along the centerline, respectively. The external loads per unit length include the normal force per unit length $p\mathbf{n}$ generated by surface tension p (including the contributions from the two sides of the soap film) and the hydrodynamic damping force per unit length $\mathbf{f}_\mathrm{h}$ exerted by the soap film on the rod. The right-hand side terms $\rho A(\partial^2\mathbf{r}/\partial t^2)$ and $\rho I\mathbf{n} \times (\partial^2\mathbf{n}/\partial t^2)$ correspond to the translational inertia force and the rotational inertia moment per unit length, respectively.

For thin rods, the rotational inertia term is smaller than the bending term by a factor $(a/R)^2 \ll 1$, where a is the cross-section radius and R is the characteristic length scale (e.g., the rod loop radius) of the thin rods (see detailed arguments and Eq. (A.1) in Appendix A). In our experiments, $a \approx 0.1$ mm and $R \approx 4.5$ cm, giving $(a/R)^2 = \mathcal{O}(10^{-6})$, which justifies neglecting the rotational inertia term $\rho I\mathbf{n} \times (\partial^2\mathbf{n}/\partial t^2)$ in Eq. (1). Accordingly, in the present work, the governing equations reduce to the classical elastica form and become

$$\frac{\partial \mathbf{F}}{\partial s} + p\mathbf{n} + \mathbf{f}_\mathrm{h} = \rho A \frac{\partial^2 \mathbf{r}}{\partial t^2} \quad \text{and} \quad \frac{\partial \mathbf{M}}{\partial s} + \mathbf{t} \times \mathbf{F} = \mathbf{0}. \tag{2}$$

The damping force per unit length $\mathbf{f}_\mathrm{h}$ is approximated by an effective anisotropic local drag law for slender bodies, linear in velocity [67–70]:

$$\mathbf{f}_\mathrm{h} = -\left(\zeta_\parallel \mathbf{t}\mathbf{t} + \zeta_\perp \mathbf{n}\mathbf{n}\right) \cdot \frac{\partial \mathbf{r}}{\partial t}, \tag{3}$$

where $\zeta_\parallel$ and $\zeta_\perp$ are the tangential and normal drag coefficients (unit: N s/m^2), respectively. The rod experiences anisotropic hydrodynamic resistance, with the damping dominated by the viscosity of the soap film. At room temperature, the viscosity of air is $\mu_\mathrm{air} = 0.018 \times 10^{-3}$

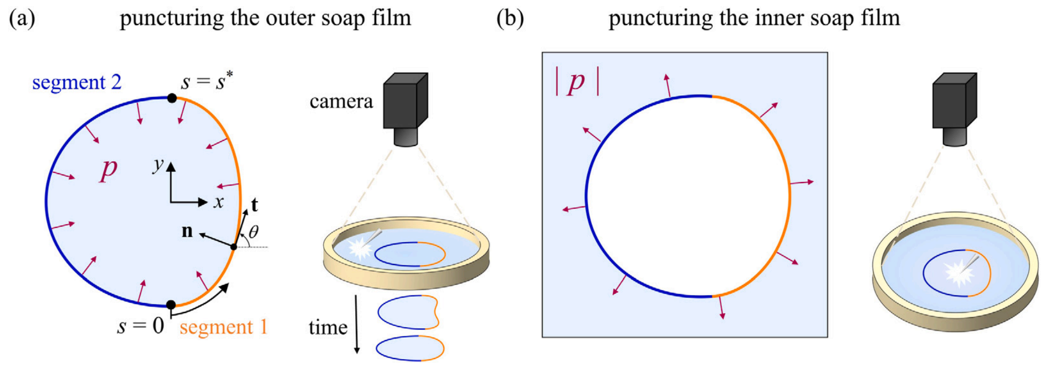

Fig. 1. Schematic of an elastic rod loop composed of two segments (1 and 2, shown in orange and blue, respectively) under inner (a) or outer (b) surface tension p, together with the corresponding experimental setups. (a) $p > 0$: the outer soap film is punctured and the remaining inner film (blue region) drives the loop contraction and oscillation. (b) $p < 0$: the inner film is punctured and the outer film (blue region) drives loop expansion and oscillation. The loop centerline is parameterized by the arclength s, increasing counterclockwise. The unit tangent $\mathbf{t}$ and normal $\mathbf{n}$ vectors are defined along s, with θ denoting the angle between $\mathbf{t}$ and the x-axis. The interfaces between the two segments are located at $s = 0$ and $s = s^*$.

Pa s [71], whereas that of the soap film is $\mu_{\text{film}} = 1.16 \times 10^{-3}$ Pa s to 2.13×10^{-3} Pa s [72]. In addition, we measured the viscosity of our soap solution using a XIUILAB NDJ-5Spro rotational viscometer at 25 °C and 60 rpm, obtaining $\mu_{\text{film}} = 2.68 \times 10^{-3}$ Pa s, consistent with reported values. The two-order-of-magnitude difference implies that the contribution from the surrounding air is negligible.

We define the drag anisotropy ratio as $\gamma = \zeta_{\parallel}/\zeta_{\perp}$. For slender rods, the drag associated with the normal direction is expected to exceed that in the tangential direction [73–75]. As rigorous determination of γ is not available for the present system, we perform a sensitivity analysis (not shown here), which demonstrates that varying γ over a broad range from 0 to 1 has a negligible influence on the resulting loop configurations. We therefore adopt $\gamma = 1/2$ in this work.

To further assess the validity of the drag formulation, we estimate the flow regime and time scales. Using the measured fluid properties (density $\rho_{\text{film}} = 1010$ kg/m^3 and viscosity $\mu_{\text{film}} = 2.68 \times 10^{-3}$ Pa s) and a characteristic velocity $U_{\text{film}} = 0.088$ m/s obtained from high-speed imaging, the Reynolds number is estimated as $\text{Re} = \rho_{\text{film}} U_{\text{film}} h_{\text{film}} / \mu_{\text{film}} \approx 0.1$ to 0.332, taking the film thickness h_{film} of 3 μm to 10 μm [72] as the relevant length scale for velocity gradients. This places the flow in a low-Reynolds-number regime, although it is not deeply in the asymptotic Stokes limit. The applicability of the instantaneous drag formulation is governed primarily by the separation of time scales rather than the Reynolds number. The dominant viscous response arises from shear across the thin film, with a characteristic diffusion time $\rho_{\text{film}} h_{\text{film}}^2 / \mu_{\text{film}}$ of about 3.4 μs to 37.7 μs, which is much smaller than the characteristic timescale of the rod motion (∼ms). This time separation indicates that the fluid adjusts rapidly to the rod motion, thereby justifying the use of a quasi-steady, instantaneous drag approximation.

The internal force $\mathbf{F}$ can be expressed in either the Cartesian basis or the local $\{\mathbf{t}, \mathbf{n}\}$ basis as

$$\mathbf{F} = F_x \mathbf{e}_x + F_y \mathbf{e}_y \quad \text{or} \quad \mathbf{F} = F_{\text{t}} \mathbf{t} + F_{\text{n}} \mathbf{n}, \tag{4}$$

where $F_x = \mathbf{F} \cdot \mathbf{e}_x$, $F_y = \mathbf{F} \cdot \mathbf{e}_y$, $F_{\text{t}} = \mathbf{F} \cdot \mathbf{t}$, and $F_{\text{n}} = \mathbf{F} \cdot \mathbf{n}$. Here, F_{t} and F_{n} represent the axial (tangential) and shear (normal) components of the internal force, respectively. The components in these two coordinate systems are related by $F_{\text{t}} = F_x \cos\theta + F_y \sin\theta$ and $F_{\text{n}} = -F_x \sin\theta + F_y \cos\theta$.

By projecting the vector force- and moment-balance equations (2) onto the local frame $\{\mathbf{t}, \mathbf{n}\}$, the scalar component equations for F_{t} and F_{n} can be derived as

$$\frac{\partial F_{\text{t}}}{\partial s} - \kappa F_{\text{n}} - \zeta_{\parallel} \mathbf{t} \cdot \frac{\partial \mathbf{r}}{\partial t} = \rho A \mathbf{t} \cdot \frac{\partial^2 \mathbf{r}}{\partial t^2}, \tag{5}$$

$$\kappa F_{\text{t}} + \frac{\partial F_{\text{n}}}{\partial s} + p - \zeta_{\perp} \mathbf{n} \cdot \frac{\partial \mathbf{r}}{\partial t} = \rho A \mathbf{n} \cdot \frac{\partial^2 \mathbf{r}}{\partial t^2}, \tag{6}$$

$$F_{\text{n}} = -\frac{\partial (B\kappa)}{\partial s}, \tag{7}$$

where the relations $\mathrm{d}\mathbf{t}/\mathrm{d}s = \kappa \mathbf{n}$ and $\mathrm{d}\mathbf{n}/\mathrm{d}s = -\kappa \mathbf{t}$ have been used. Eq. (7) directly yields F_{n}. Substituting Eq. (7) into Eq. (6) permits the derivation of F_{t}.

We introduce nondimensional quantities (denoted by a tilde)

$$\tilde{s} = \frac{s}{R} \in [0, 2\pi], \quad \tilde{\mathbf{r}} = \frac{\mathbf{r}}{R}, \quad \tilde{\mathbf{M}} = \frac{R}{B_1}\mathbf{M}, \quad \tilde{\mathbf{F}} = \frac{R^2}{B_1}\mathbf{F}, \quad \tilde{\rho} = \frac{\rho}{\rho_1},$$
$$\tilde{p} = \frac{R^3}{B_1} p, \quad \tilde{t} = \frac{t}{R^2}\sqrt{\frac{B_1}{\rho_1 A}}, \quad \tilde{\zeta}_{\perp} = \frac{R^2}{\sqrt{B_1 \rho_1 A}} \zeta_{\perp}, \tag{8}$$

where $R = L/(2\pi)$ is the effective rod loop radius, and B_1 and ρ_1 denote the stiffness and density of the rod segment 1, respectively. For homogeneous rods, B_1 and ρ_1 are equal to the uniform stiffness B and density ρ, respectively. With this nondimensionalization, Eq. (2) becomes

$$\frac{\partial \tilde{\mathbf{F}}}{\partial \tilde{s}} + \tilde{p}\mathbf{n} + \tilde{\mathbf{f}}_{\text{h}} = \tilde{\rho} \frac{\partial^2 \tilde{\mathbf{r}}}{\partial \tilde{t}^2} \quad \text{and} \quad \frac{\partial \tilde{\mathbf{M}}}{\partial \tilde{s}} + \mathbf{t} \times \tilde{\mathbf{F}} = 0, \tag{9}$$

where the normalized damping force is $\tilde{\mathbf{f}}_{\text{h}} = -\tilde{\zeta}_{\perp}(\gamma \mathbf{t}\mathbf{t} + \mathbf{n}\mathbf{n}) \cdot (\partial \tilde{\mathbf{r}}/\partial \tilde{t})$.

Introducing the normalized coordinates $\tilde{x} = \tilde{\mathbf{r}} \cdot \mathbf{e}_x$ and $\tilde{y} = \tilde{\mathbf{r}} \cdot \mathbf{e}_y$ of the rod centerline and the normalized components $\tilde{F}_x = \tilde{\mathbf{F}} \cdot \mathbf{e}_x$ and $\tilde{F}_y = \tilde{\mathbf{F}} \cdot \mathbf{e}_y$ of the internal force, the normalized geometrical and governing equations (2) of the system are expressed as

$$\frac{\partial \tilde{x}}{\partial \tilde{s}} = \cos\theta, \quad \frac{\partial \tilde{y}}{\partial \tilde{s}} = \sin\theta, \tag{10}$$

$$\frac{\partial \tilde{F}_x}{\partial \tilde{s}} - \tilde{p}\sin\theta - \tilde{\zeta}_{\perp}\left[(\gamma\cos^2\theta + \sin^2\theta)\frac{\partial \tilde{x}}{\partial \tilde{t}} + (\gamma - 1)\sin\theta\cos\theta\frac{\partial \tilde{y}}{\partial \tilde{t}}\right] = \tilde{\rho}\frac{\partial^2 \tilde{x}}{\partial \tilde{t}^2}, \tag{11}$$

$$\frac{\partial \tilde{F}_y}{\partial \tilde{s}} + \tilde{p}\cos\theta - \tilde{\zeta}_{\perp}\left[(\gamma - 1)\sin\theta\cos\theta\frac{\partial \tilde{x}}{\partial \tilde{t}} + (\gamma\sin^2\theta + \cos^2\theta)\frac{\partial \tilde{y}}{\partial \tilde{t}}\right] = \tilde{\rho}\frac{\partial^2 \tilde{y}}{\partial \tilde{t}^2}, \tag{12}$$

$$\frac{\partial}{\partial \tilde{s}}\left(\frac{B}{B_1}\frac{\partial \theta}{\partial \tilde{s}}\right) - \tilde{F}_x \sin\theta + \tilde{F}_y \cos\theta = 0. \tag{13}$$

In the undamped limit, $\tilde{\zeta}_{\perp} = 0$. For homogeneous rods of constant bending stiffness ($B_1 = B$), Eq. (13) simplifies to $\partial^2\theta/\partial\tilde{s}^2 - \tilde{F}_x \sin\theta + \tilde{F}_y \cos\theta = 0$.

2.2. Boundary conditions and initial conditions

For the closed rod loop, its position $\mathbf{r}(s,t)$, tangent angle $\theta(s,t)$, moment $\mathbf{M}(s,t)$, and internal force $\mathbf{F}(s,t)$ are continuous. The periodic boundary conditions at $s = 0$ are

$$\mathbf{r}(L,t) = \mathbf{r}(0,t), \quad \theta(L,t) = \theta(0,t) + 2\pi, \quad \mathbf{M}(L,t) = \mathbf{M}(0,t),$$
$$\text{and} \quad \mathbf{F}(L,t) = \mathbf{F}(0,t). \tag{14}$$

For a homogeneous rod loop with uniform bending stiffness, the continuity of moment $\mathbf{M}(= B\kappa\mathbf{t} \times \mathbf{n})$ requires the curvature continuity $\kappa(L,t) = \kappa(0,t)$. In contrast, if the loop is piecewise homogeneous, composed of two uniform segments joined at $s = 0$ and s^*, continuity of the bending moment permits curvature discontinuities at the interfaces, satisfying $\kappa_2(L,t)/\kappa_1(0,t) = B_1/B_2$ and $\kappa_2(s^*,t)/\kappa_1(s^*,t) = B_1/B_2$, where the subscripts 1 and 2 denote quantities associated with segments 1 and 2, respectively.

Eqs. (10)–(13) are discretized using a finite-difference scheme, with the details of the discretization provided in Appendix B. The resulting nonlinear system is solved iteratively using the Newton–Raphson method.

2.3. Power balance

To clarify the role of soap-film viscosity in the dynamics, which is inherently present in experiments and practical realizations, we formulate a power-balance relation for the coupled rod–film system. The evolution of the loop configuration is governed by the interplay among bending energy E_b, surface energy E_t, kinetic energy E_k, and the rate P_d of energy dissipation due to viscous damping of the remaining soap film.

The bending energy of the rod loop is $E_b = \int_0^L (B\kappa^2/2)\mathrm{d}s$. The surface-tension energy is $E_t = pA_{\text{film}}$, where A_{film} is the area of the remaining film. If the outer soap film is punctured, $A_{\text{film}} = A_{\text{enclosed}}$, where the enclosed area inside the loop is $A_{\text{enclosed}} = (1/2)\oint(x\mathrm{d}y - y\mathrm{d}x) = (1/2)\int_0^L (x\sin\theta - y\cos\theta)\mathrm{d}s$. If the inner film is punctured, $A_{\text{film}} = A_{\text{frame}} - A_{\text{enclosed}}$, where A_{frame} is the area bounded by the rigid outer frame. The kinetic energy of the loop is $E_k = (1/2)\int_0^L \rho A(\partial\mathbf{r}/\partial t)^2\mathrm{d}s$.

The power balance of the system reads

$$\frac{\mathrm{d}}{\mathrm{d}t}(E_b + E_t + E_k) = -P_d(t), \tag{15}$$

where the instantaneous dissipation rate $P_d(t)$ due to viscous drag from the soap film is

$$P_d(t) = -\int_0^L \left(\mathbf{f}_h \cdot \frac{\partial\mathbf{r}}{\partial t}\right)\mathrm{d}s. \tag{16}$$

We can further introduce the accumulated dissipated energy $E_d = \int_0^t P_d(t')\mathrm{d}t'$, and $\mathrm{d}(E_b + E_t + E_k + E_d)/\mathrm{d}t = 0$.

At the final equilibrium state ($\partial\mathbf{r}/\partial t = 0$), viscous dissipation vanishes and the configuration minimizes $E_b + E_t$.

3. Experiments

In addition to numerical calculations, we experimentally examined the dynamic instability of the elastic rod loops. Both homogeneous and inhomogeneous loops were fabricated from 304 stainless steel thin rods. The homogeneous loop was constructed by bonding the ends of a single rod with an ultraviolet (UV)-curable adhesive to form a closed loop; the rod exhibited a measured bending stiffness of $B = 2.27 \times 10^{-6}\,\mathrm{N\ m^2}$. The inhomogeneous loops consisted of two rods of equal length and identical density but different bending stiffnesses: $B_1 = 6.13 \times 10^{-7}\,\mathrm{N\ m^2}$ and $B_2 = 7.85 \times 10^{-6}\,\mathrm{N\ m^2}$, corresponding to a stiffness ratio $B_2/B_1 = 12.8$. These two segments were joined end-to-end using the same UV-curable adhesive to form a closed loop.

Each rod loop was first mounted within a soap film and allowed to equilibrate. The homogeneous loop exhibited an initially circular shape, whereas the shape of the inhomogeneous loop depended on the stiffness ratio B_2/B_1 and deviated from a circle. The loop lay in the plane of the soap film and divided it into inner and outer regions. Puncturing either region created a sudden traction or pressure imbalance across the loop and initiated the dynamic instability (Fig. 1). When the outer film was punctured, the rod loop was no longer supported by the rigid frame and moved downward under gravity while undergoing in-plane buckling and oscillation; when the inner film was punctured, the remaining outer film stayed attached to the frame and continued to support the loop. The resulting loop deformation was recorded using a Phantom C211 high-speed camera operating at 1800 frames per second.

4. Dynamical buckling of a homogeneous elastic rod loop

This section examines the dynamics of a homogeneous elastic loop, identifies the fundamental deformation mechanisms, and provides a reference for subsequent comparison with inhomogeneous cases. We first analyze the undamped response at low pressure (Section 4.1), then examine multimodal deformation at high pressure in the absence of dissipation (Section 4.2), and finally incorporate soap-film viscosity to quantify the experimentally observed damping and oscillatory behavior, and to elucidate the underlying mechanisms (Section 4.3). From this section onward, we follow conventional usage and use “pressure” to denote the effective normal loading induced by surface tension.

4.1. Periodic oscillation under low pressure in the absence of dissipation

The classical static buckling analysis of a circular loop predicts the critical buckling pressure $\tilde{p}_{cr} = n^2 - 1$ for the azimuthal deformation mode n [18]. However, this static criterion does not account for inertial effects or time-dependent evolution. To characterize the onset of dynamic instability in the absence of dissipation, we instead perform a linear stability analysis of a homogeneous circular rod loop under pressure $\tilde{p}$. Following the theoretical framework in Ref. [60], infinitesimal perturbations of the form $e^{in\tilde{s}+\tilde{\omega}\tilde{t}}$ are introduced to the circular base state, where $\tilde{\omega}$ in general is a complex number denoting the temporal growth rate and n is the azimuthal deformation mode number corresponding to the number of lobes along the loop. This perturbation ansatz leads to the dispersion relation [60]

$$\tilde{\omega}^2 = \frac{n^2(n^2-1)}{n^2+1}(\tilde{p} + 1 - n^2). \tag{17}$$

For a given $\tilde{p}$, all modes satisfying $2 \le n < \sqrt{\tilde{p}+1}$ are linearly unstable. Among these unstable modes ($\tilde{\omega} > 0$), the mode n with the largest growth rate $\tilde{\omega}$ dominates the initial dynamic buckling behavior of the loop. To demonstrate this, Fig. 2a shows $\tilde{\omega}^2$ as a function of $\tilde{p}$ for various modes n. The upper envelope (solid line), formed by the intersections of individual mode branches (dashed lines), identifies the most unstable mode at each pressure.

The corresponding discrete mode selection map (Fig. 2b) specifies the pressure intervals over which each mode n is most favored initially. It should be emphasized that the linear prediction applies only to the onset of instability and characterizes the earliest deformation pattern, rather than the final lobe number after nonlinear evolution.

We consider the low-pressure case with $\tilde{p} = 3.8$, where the outer film is punctured while the inner film remains intact. This value lies within the range of dynamic buckling pressure for mode 2 (Fig. 2b). Under such weak loading, the rod loop in the absence of dissipation undergoes sustained periodic oscillations. Fig. 3a illustrates the time evolution of the loop configuration. Small spatial perturbations are introduced to the initially circular loop to trigger instability.

Upon the application of $\tilde{p}$, the loop undergoes cyclic concave-to-convex shape transformations, evolving from a circular to an elliptical and then to a dumbbell-like profile (half cycle), followed by a reverse deformation back toward the circular configuration in the next half cycle. This periodic motion corresponds to the $n = 2$ buckling mode

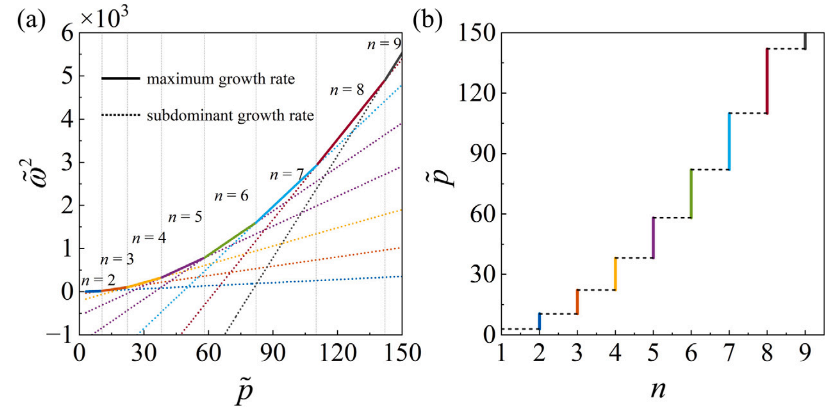

Fig. 2. The most unstable buckling modes at the onset of instability based on Eq. (17). (a) Squared normalized growth rate $\tilde{\omega}^2$ versus normalized pressure $\tilde{p}$ for different modes n. Solid line: maximum growth rate, identifying the most unstable mode at each pressure. Dashed lines: subdominant growth rates. The labels indicate the corresponding mode numbers. (b) The most unstable mode n as a discrete function of $\tilde{p}$, showing the pressure intervals over which each buckling mode is initially preferred.

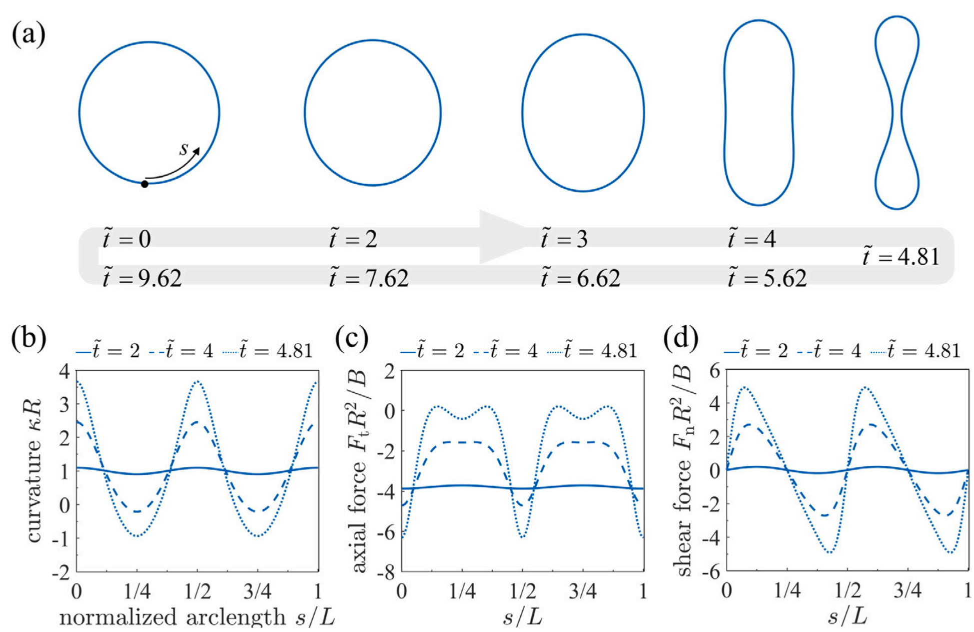

Fig. 3. Temporal evolution of the loop configuration, curvature profile, and internal force distributions for the homogeneous elastic rod loop at low pressure $\tilde{p}$ = 3.8 in the absence of viscous dissipation. (a) Evolution of the loop configuration over one oscillation cycle at normalized time $\tilde{t}$ = 0(9.62), 2(7.62), 3(6.62), 4(5.62), and 4.81. The normalized oscillation period is T = 9.62. (b) Evolution of the curvature distribution along the loop at selected times $\tilde{t}$ = 2, 4, and 4.81. (c,d) Spatial distributions of the normalized axial and shear forces, $F_t R^2/B$ and $F_n R^2/B$. A positive (negative) F_t indicates tensile (compressive) axial force, while a positive F_n points toward the loop interior.

(Fig. 2), characterized by an elliptical shape with two alternating lobes of curvature around the loop. In the absence of damping, this mode remains stable and persists indefinitely under ideal inviscid conditions.

The $n = 2$ buckling mode is also evident in the periodic curvature and force distributions (Fig. 3b,c). As indicated by Eq. (7), $F_n = 0$ at curvature extrema where $(\partial\kappa/\partial s = 0)$, occurring at $s/L = 0, 1/4, 1/2$, and 3/4 (Fig. 3c). The axial force F_t attains its extrema at locations where the spatial gradient of F_n is largest.

Taking the initial equilibrium configuration as the ground energy state, Fig. 4 presents the temporal evolution of the energy change with components ΔE_b, ΔE_t, and E_k over three oscillation periods. For the initial circular configuration, the ground bending and surface energies are $E_{b0} = 2\pi^2 B/L$ and $E_{t0} = pL^2/(4\pi)$, respectively. Accordingly, the bending and surface energy changes are $\Delta E_b = E_b - 2\pi^2 B/L$ and $\Delta E_t = E_t - pL^2/(4\pi)$. Under weak driving (low normalized pressure), the motion is slow and the kinetic energy E_k is much smaller than ΔE_b and ΔE_t. During each cycle, ΔE_b and ΔE_t oscillate out of phase: inward bending increases ΔE_b but decreases ΔE_t through the reduction of enclosed area. Maximum deformation occurs at zero velocity, with minimal surface area and maximal bending energy. The periodic concave–convex oscillation is thus driven by the reciprocal exchange between bending and surface energies in the absence of dissipation.

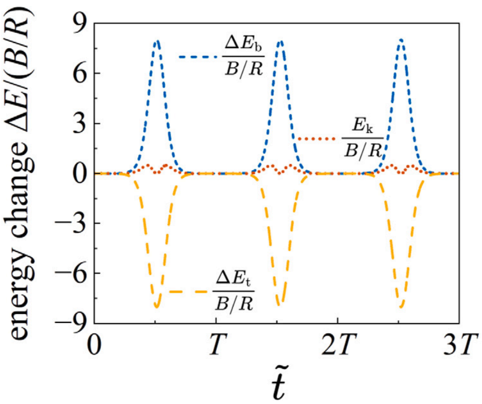

Fig. 4. Temporal evolution of the energy change for the undamped homogeneous elastic rod loop at $\tilde{p} = 3.8$ in the absence of viscous dissipation, corresponding to the case shown in Fig. 3. The normalized energy components include the bending energy change $\Delta E_b/(B/R)$, surface energy change $\Delta E_t/(B/R)$, and kinetic energy $E_k/(B/R)$, all measured relative to the initial equilibrium configuration taken as the ground state.

4.2. Multimodal deformation of a homogeneous rod loop under high pressure in the absence of dissipation

At high pressure, the rod loop undergoes multimodal buckling instability. Fig. 5 illustrates the shape evolution of homogeneous circular loops at $\tilde{p} = 16, 32, 64$, and 128. The top row shows the evolving loop configurations, where solid circles indicate the location of $s = 0$.

The middle and bottom rows present the distributions of the normalized axial and shear internal forces at the final frame of each sequence in Fig. 5. The axial force F_t alternates between tension and compression along the loop. At low pressure (e.g., $\tilde{p} = 16$), F_t follows a clear three-periodic pattern, whereas at higher pressures (e.g., $\tilde{p} = 32, 64$, and 128) it becomes increasingly irregular, signaling enhanced nonlinear mode coupling. Notably, at $\tilde{p} = 128$, three local peaks of F_t emerge within specific inter-crest regions, suggesting localized interference and energy transfer between adjacent high-order modes. Collectively, these observations provide compelling evidence that neighboring deformation features coalesce into composite lobes through nonlinear interactions and geometric constraints at elevated $\tilde{p}$.

Based on the theoretical prediction in Eq. (17), the most unstable mode numbers corresponding to $\tilde{p} = 16, 32, 64$, and 128 are $n = 3$, 4, 6, and 8, respectively (Fig. 2b). However, the modes observed at later stages of the post-buckling evolution in Fig. 5 are $n = 3$, 4, 5, and 6. As detailed in Appendix C (see, e.g., the case $\tilde{p} = 64$), the initial mode selection remains consistent with the linear prediction, whereas the subsequent reduction in the mode number is a nonlinear effect associated with lobe coalescence and lobe collapse (Fig. C.1 in Appendix C), in which neighboring lobes merge or a central lobe collapses within a local multi-lobe structure. These processes redistribute deformation and reduce the mode number during the nonlinear stage. Similar reductions from initially excited high-order modes to lower-order configurations have been reported in dynamically buckled rods and filaments, where post-buckling evolution can involve mode coarsening [63,76–79].

4.3. Effects of film dissipation on deformation of a homogeneous rod loop

Besides the dissipation-free theoretical analysis presented in the previous sections, we now experimentally and numerically examine how film viscosity influences the dynamic response of a homogeneous rod loop (Fig. 6). In the experiments here, dynamic instability was triggered by puncturing the outer soap film. A pronounced oscillatory configurational response was observed: the loop reached its maximum contraction at 34 ms, subsequently rebounded, and underwent small-amplitude, decaying oscillations. By 78 ms, the loop nearly returned to its equilibrium shape (Fig. 6a).

Fig. 6b presents the numerical results. For a meaningful comparison with the experiments, a consistent definition of the time origin is required. In the experiments, time is effectively measured from the onset of visible deformation, whereas in the simulations a finite growth stage from a round initial configuration precedes observable motion. We therefore shift the simulation time axis for comparison, taking the onset of visible deformation (around $\tilde{t} \approx 1.7$, indicated by the open circle on the time axis) as the reference point. With this alignment, the experimental and numerical time scales exhibit a consistent ratio of about 10 ms, in agreement with a ratio of about 12 ms predicted by the time scaling relation in Fig. 6.

Fig. 7a presents the temporal evolution of the energy change, with the initial equilibrium configuration taken as the ground energy state. Under low pressure, the motion is slow and the kinetic energy E_k remains much smaller than the changes in bending and tension energies, ΔE_b and ΔE_t, which oscillate out of phase with gradually decreasing amplitudes. The accumulated dissipated energy E_d and the kinetic energy E_k saturate significantly earlier than ΔE_b and ΔE_t, indicating that the dynamic process quickly transitions into a slow regime, during which the compensation between bending and tension energies proceeds very slowly, consistent with the trend of $P_d(t)$ observed in Fig. 7b. The profile of the instantaneous dissipation rate $P_d(t)$ features a sharp initial peak followed by smaller ones, indicating that most viscous energy loss occurs during the first contraction–rebound cycle.

5. Dynamical buckling of inhomogeneous thin rod loops

Having established the dynamic characteristics of a homogeneous loop, we now investigate the dynamics of inhomogeneous loops composed of two segments with contrasting bending stiffnesses or densities, or both. Such spatial inhomogeneity reduces the degree of circumferential symmetry of the loop and leads to more intricate mode selection during surface-tension-driven motion. Specifically, we first analyze how stiffness inhomogeneity modifies the critical buckling pressure (Section 5.1), then investigate how stifffness inhomogeneity (Sections 5.2–5.4) and density inhomogeneity (Section 5.5) affect the transient and oscillatory dynamics, and finally examine the combined effects of stiffness and density inhomogeneities on multimodal deformation (Section 5.6).

5.1. Critical buckling pressure of stiffness-inhomogeneous rods

For stiffness-inhomogeneous rod loops, obtaining an analytical dispersion relation for the dynamic instability is generally intractable. Nevertheless, the onset of instability in the dynamic regime is expected to correlate with the corresponding static buckling threshold: once the applied pressure exceeds the critical value, the elastic loop becomes unstable and undergoes subsequent dynamic evolution. Motivated by this, we first determine the critical buckling pressure from a static analysis, which serves as a reference criterion for the onset of instability in the dynamic simulations.

We consider a composite elastic rod loop comprising two segments with distinct bending stiffnesses, B_1 and B_2. The stiffness difference causes the equilibrium shape to deviate from a perfect circle.

To determine the critical buckling pressure initiating the instability, we use a constrained energy minimization approach under an area constraint, in which the enclosed area of the loop is fixed slightly below its load-free value. Specifically, the bending energy of the rod loop E_b is minimized subject to the constraint of the loop's enclosed area $A_{\text{enclosed}} = \alpha A_0$, where A_0 denotes the enclosed area at $p = 0$. The critical buckling pressure is then obtained as $p_{\text{cr}} = \lim_{\alpha \to 1} p(\alpha)$. Details of the numerical procedure are provided in Appendix D.

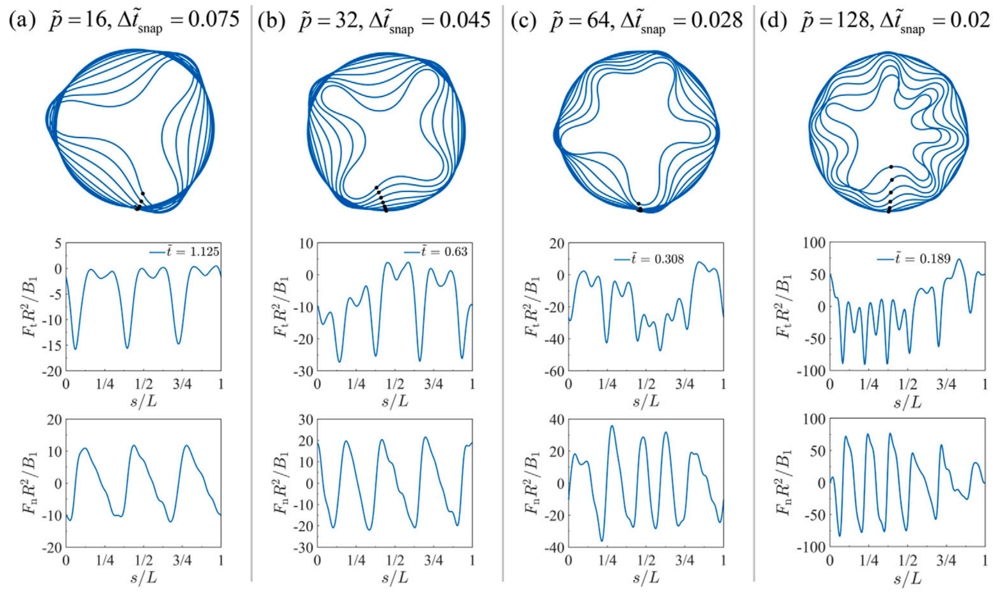

Fig. 5. Configurations and internal force profiles of a homogeneous rod loop at different values of the normalized pressure $\tilde{p}$. Panels (a)–(d) correspond to $\tilde{p}$ = 16, 32, 64, and 128, respectively. The total simulation times are 1.125, 0.63, 0.308, and 0.189, respectively, and $\Delta\tilde{t}_{\mathrm{snap}}$ denotes the time interval between successive configuration snapshots. Top row: successive configuration snapshots during the deformation process; solid circles mark the location $s = 0$ and s increases counterclockwise. For each $\tilde{p}$, the middle and bottom rows show the axial and shear force profiles evaluated at the final time corresponding to the most deformed configuration shown in the top row.

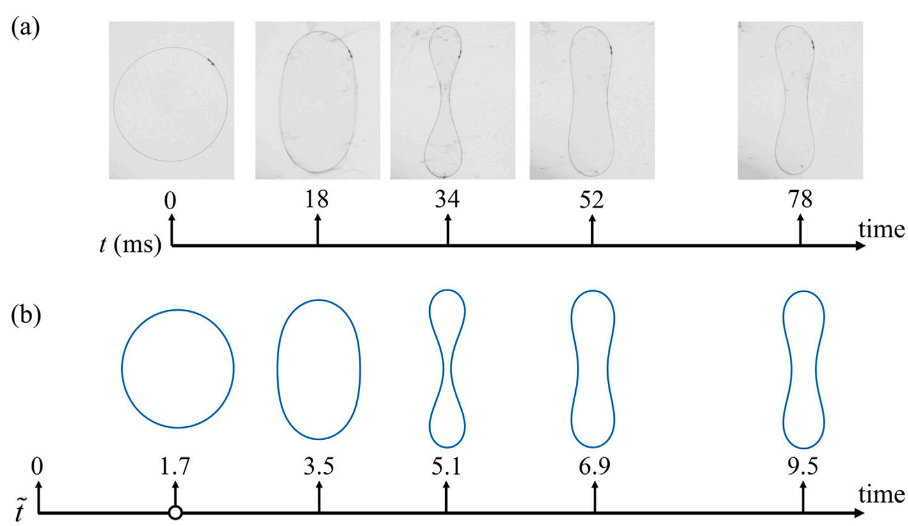

Fig. 6. Oscillatory configurational response of a homogeneous rod loop following the rupture of the outer soap film. (a) Experimental measurements. (b) Numerical simulations at normalized pressure $\tilde{p} = 4.3$ and normal drag coefficient $\tilde{\zeta}_{\perp} = 1.2$. In (b), the open circle at $\tilde{t} = 1.7$ marks the onset of visible deformation, which defines the time origin used for comparison with the experiments.

Fig. 8 shows the dependence of the normalized critical buckling pressure $\tilde{p}_{\mathrm{cr}}(B_2/B_1, k)$ on the stiffness ratio B_2/B_1 and the arclength fraction $k \in (0,1)$ of segment 1 for two-segment rod loops. Since the pressure is normalized by B_1, for the two-segment system exchanging the segment labels corresponds to replacing k with $1-k$, leading to the reciprocity relation

$$\tilde{p}_{\mathrm{cr}}\left(\frac{B_2}{B_1}, k\right) = \frac{B_2}{B_1}\tilde{p}_{\mathrm{cr}}\left(\frac{B_1}{B_2}, 1-k\right), \tag{18}$$

which provides a stringent consistency check for the numerical results.

Together with the condition that $\tilde{p}_{\mathrm{cr}}(B_2/B_1, k) \to 0$ as $B_2/B_1 \to \infty$ for any fixed $k \in (0,1)$, Eq. (18) implies another asymptotic behavior: $\tilde{p}_{\mathrm{cr}}(B_2/B_1, k) \to 0$ as $B_2/B_1 \to 0$. Therefore, for each fixed k, $\tilde{p}_{\mathrm{cr}}(B_2/B_1, k)$ approaches zero at both extremes of stiffness contrast and remains positive in between. Assuming $\tilde{p}_{\mathrm{cr}}(B_2/B_1, k)$ is continuous in B_2/B_1, it must be non-monotonic in B_2/B_1, whereas no such constraint applies with respect to k.

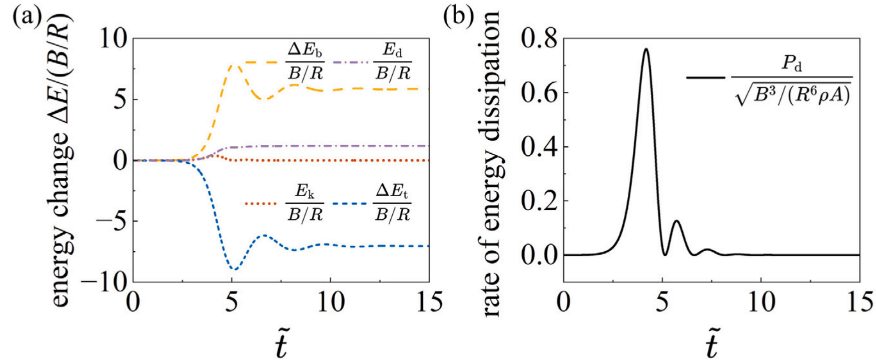

Fig. 7. Temporal evolution of the energy change (a) and dissipation rate (b) for the homogeneous elastic rod loop at normalized pressure $\tilde{p} = 4.3$, where $E_d/(B/R)$ is the normalized accumulated dissipated energy and P_d is the instantaneous dissipation rate obeying Eq. (15). Numerical results in (a) confirm energy conservation $d(\Delta E_b + \Delta E_t + E_k + E_d)/dt = 0$.

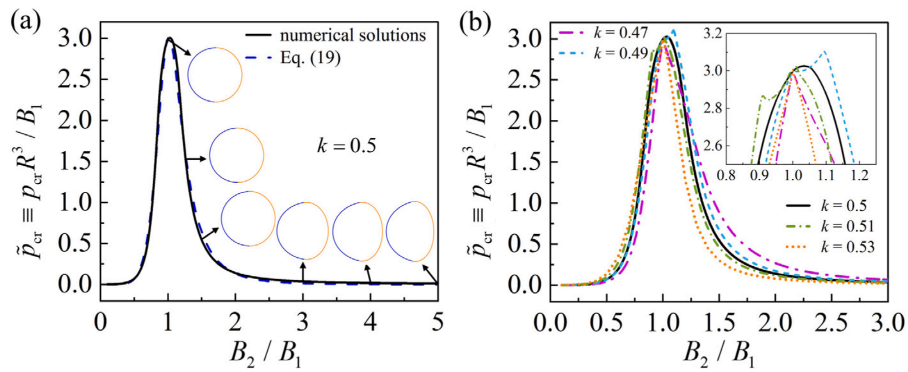

Fig. 8. Critical buckling pressure $\tilde{p}_{cr} = p_{cr}R^3/B_1$ as functions of the stiffness ratio B_2/B_1 and arclength fraction k of segment 1 for two-segment rod loops, with segment 2 occupying the remaining fraction $1-k$. (a) Equal-length case ($k = 0.5$). The insets show the corresponding equilibrium configurations at $B_2/B_1 = 1$, 1.25, 1.5, 3, 4, and 5, with the orange and blue parts denoting segments 1 and 2, respectively. (b) Unequal-length cases with $k = 0.47$, 0.49, 0.51, and 0.53; $k = 0.5$ is included for reference. The inset in (b) shows a zoom-in of the peak region.

For the equal-length case ($k = 1/2$, Fig. 8a), the numerical results are well captured by the following reciprocal-symmetric fitting function:

$$\tilde{p}_{cr}\left(\frac{B_2}{B_1}, \frac{1}{2}\right) \equiv \frac{p_{cr}R^3}{B_1} = \frac{6\sqrt{B_2/B_1}}{(B_2/B_1)^6 + (B_2/B_1)^{-6}}. \tag{19}$$

The exponent in Eq. (19) is taken as 6 for simplicity, which provides an excellent fit to the data, with a coefficient of determination of 0.9963. A closer examination of the numerical results in Fig. 8a indicates that the maximum critical pressure $\tilde{p}_{cr} \approx 3.025$ occurs at $B_2/B_1 = 1.04$, slightly exceeding $\tilde{p}_{cr} = 3$ for a homogeneous loop ($B_2/B_1 = 1$).

When k slightly deviates from 1/2, more complex profiles of $\tilde{p}_{cr}(B_2/B_1, k)$ are observed. For $k = 0.49$ and 0.51, two local maxima emerge, with peak values of $\tilde{p}_{cr}$ exceeding 3; in contrast, for $k = 0.47$, the maximum $\tilde{p}_{cr}$ remains close to $\tilde{p}_{cr} = 3$, consistent with the homogeneous case (attained at $B_2/B_1 = 1$).

Away from these peak regions, $\tilde{p}_{cr}$ decreases sharply as the stiffness contrast increases. This reduction can be attributed to localized flattening of the softer segment, which forms a shallow arch-like region with reduced resistance to transverse loading. Comparable effects have been reported for pipes under external pressure, where material inhomogeneity can modify collapse patterns and significantly reduce structural capacity [1].

5.2. Periodic oscillation of stiffness-inhomogeneous rods under relatively low pressure in the absence of dissipation

We consider the case of $\tilde{p} = 3.8$, corresponding to outer-film rupture. For a stiffness ratio $B_2/B_1 = 5$, the critical pressure for the onset of buckling, obtained from the static analysis, is $\tilde{p}_{cr} = 0.011$ (Fig. 8), far below the applied pressure $\tilde{p} = 3.8$. The rod loop therefore loses stability immediately and enters a symmetry-breaking post-buckling oscillatory state (Fig. 9a). The undamped oscillation period is strongly reduced relative to the homogeneous case (the period $T = 2.25$ versus 9.62), with deformation concentrated in the softer segment.

As shown in Fig. 9b, the stiffer segment remains in tangential compression throughout the motion, while the softer segment is also compressive during mild deformations but becomes tensile at large deformation amplitudes, especially in regions of low or negative curvature. Near the segment junction, where curvature is elevated, the compressive F_t in the softer segment becomes significantly amplified. The shear force profiles exhibit pronounced oscillatory modulations, revealing high-frequency components that reflect the intrinsically nonlinear vibrational response of stiffness-inhomogeneous loops.

Fig. 10 reveals the underlying energy-exchange mechanism driving the asymmetric oscillations of the stiffness-inhomogeneous rod loop. Unlike the homogeneous case, where oscillations appear as discrete bursts separated by intervals with only minimal variations in ΔE_b, ΔE_t, and E_k, the inhomogeneous loop exhibits a much more sinusoidal,

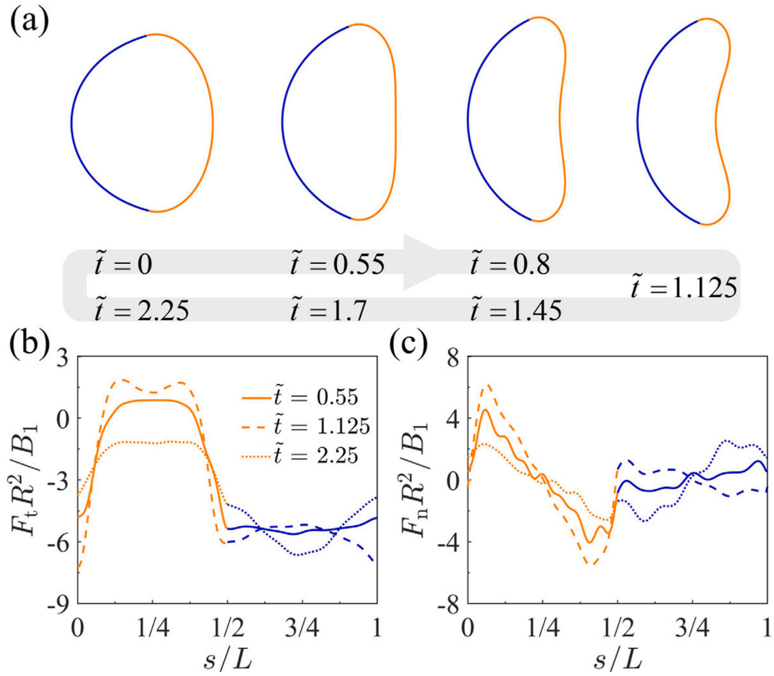

Fig. 9. Dynamic response of a stiffness-inhomogeneous rod loop (stiffer segment in blue, softer segment in orange) at normalized pressure $\tilde{p} = 3.8$ in the absence of viscous dissipation, with stiffness ratio $B_2/B_1 = 5$. (a) Loop configurations at $\tilde{t} = 0\,(2.25)$, $0.55\,(1.7)$, $0.8\,(1.45)$, and 1.125. The normalized oscillation period is $T = 2.25$. (b,c) Spatial distributions of the normalized axial and shear forces, $F_t R^2/B_1$ and $F_n R^2/B_1$, at $\tilde{t} = 0.55$, 1.125, and 2.25.

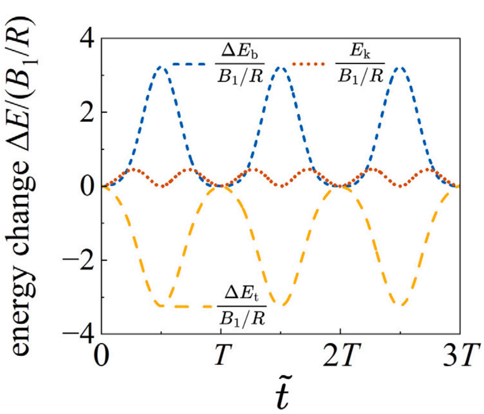

Fig. 10. Temporal evolution of the energy change for the undamped stiffness-inhomogeneous rod loop at $\tilde{p} = 3.8$ in the absence of viscous dissipation, corresponding to the case shown in Fig. 9. The normalized bending energy change $\Delta E_b/(B_1/R)$, surface energy change $\Delta E_t/(B_1/R)$, and kinetic energy $E_k/(B_1/R)$ oscillate periodically, indicating the periodic response associated with stiffness contrast.

smoothly varying oscillatory pattern. This qualitative difference arises from the substantially reduced buckling pressure associated with the large stiffness contrast: the loop loses stability almost immediately upon loading and rapidly enters a persistent post-buckling oscillatory state.

5.3. Effects of stiffness inhomogeneity on multimodal deformation under high pressure in the absence of dissipation

To assess how stiffness inhomogeneity modifies the high-pressure undamped dynamics, we examine rod loops with stiffness ratios $B_2/B_1 = 2$ and 5 (Fig. 11). Compared with the homogeneous loop, stiffness-inhomogeneous loops exhibit clear spatial segregation of deformation modes. The stiffer segment (blue) resists bending more strongly and therefore favors lower-order buckling patterns. The softer segment (orange), especially near the material junction, develops pronounced curvature variations and higher-order wavy deformations concentrated away from the junction. This modal disparity becomes increasingly pronounced as the stiffness contrast increases. The deformation in the softer segment intensifies, while the stiffer segment appears less deformed.

Lobe-number reduction is also observed, occurring through two nonlinear pathways: lobe collapse and lobe coalescence. The former, characterized by the inward collapse of a central lobe within a local multi-lobe structure, predominates at intermediate pressures in the softer segment (Fig. 11b,f), whereas the latter, involving the merging of neighboring lobes, emerges at sufficiently high pressures, occurring in both segments in Fig. 11d and primarily in the softer segment in Fig. 11g,h.

5.4. Combined effects of film dissipation and loop stiffness inhomogeneity

We now investigate the damped oscillatory response of stiffness-inhomogeneous loops composed of two rod segments of equal length and identical density but with different bending stiffnesses, $B_1 = 6.13\times10^{-7}$ N m^2 and $B_2 = 7.85\times10^{-6}$ N m^2, yielding a stiffness ratio 12.8. This configuration matches the experimental system consisting of inhomogeneous loops embedded in soap films. Following the sudden rupture of the outer film, the loop undergoes asymmetric oscillations, as shown in Fig. 12a–c through both experiments and simulations. As shown in Fig. 12a, soap-film rupture excites pronounced oscillations in the softer (right) segment, which reaches maximum contraction at 18 ms before rebounding and exhibiting small-amplitude, decaying oscillations. The motion gradually damps out and the segment settles near equilibrium by 72 ms due to viscous dissipation. In contrast, the stiffer (left) segment undergoes only minor displacement, moving slightly in the opposite direction because of its substantially higher bending resistance.

To assess how film viscosity modifies the dynamics, a thickening agent is added to the soap solution to increase viscosity. The corresponding experiment (Fig. 12b) shows that the softer segment now

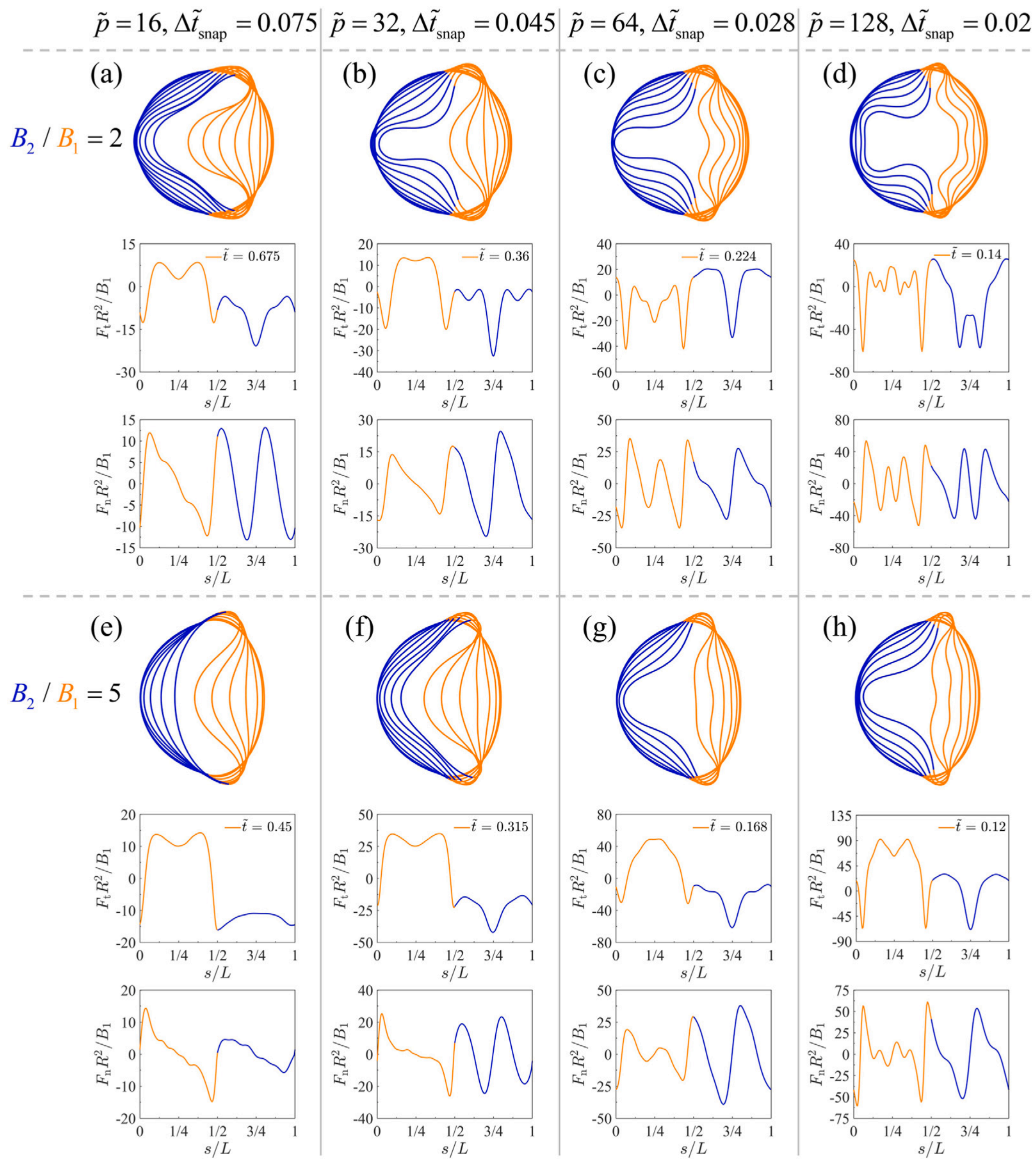

Fig. 11. Shape evolution and internal force profiles of stiffness-inhomogeneous rod loops (stiffer segment in blue, softer segment in orange) at different values of the normalized pressure $\tilde{p}$. Panels (a)–(d) correspond to the stiffness ratio $B_2/B_1 = 2$, and panels (e)–(h) correspond to $B_2/B_1 = 5$. In each panel, the upper plot shows successive configuration snapshots, and the two lower plots show the normalized axial and shear force profiles, $F_t R^2/B_1$ and $F_n R^2/B_1$, evaluated at the final time of each sequence. From left to right, the columns correspond to $\tilde{p} = 16$, 32, 64, and 128. The corresponding total simulation times are 0.675, 0.36, 0.224, and 0.14 for $B_2/B_1 = 2$, and 0.45, 0.315, 0.168, and 0.12 for $B_2/B_1 = 5$, respectively. The time interval $\Delta\tilde{t}_{\text{snap}}$ between successive configuration snapshots is indicated above each sequence. The arclength coordinate starts from the lower segment junction ($s = 0$) and increases counterclockwise.

reaches its peak contraction at 22 ms and undergoes fewer, lower-amplitude oscillations, stabilizing around 51 ms. The stiffer segment remains nearly stationary in both cases. Increased viscosity suppresses both the amplitude and frequency of oscillations, delays the peak response, and accelerates relaxation.

The simulation in Fig. 12c considers a rod loop with stiffness ratio $B_2/B_1 = 12.8$ subjected to normalized pressure $\tilde{p} = 5$ and normalized viscous drag $\tilde{\zeta}_\perp = 2$. The numerical results reproduce the experimentally observed damping behavior and capture the essential features of the stiffness-controlled oscillatory relaxation. In particular, the simulations recover the key configurations associated with the maximum contraction and the subsequent rebound, and the time interval between these two stages is also consistent in order of magnitude with the experimental observations. To quantify the damping effect, Fig. 12d plots the transverse displacement of the midpoint of the softer segment, located farthest from the junction and exhibiting the largest deflection.

Following inner-film rupture, the post-instability dynamics are shown in Fig. 13a. Both the stiffer and softer segments oscillate synchronously but with different amplitudes. The loop reaches its maximum outward displacement at 28 ms, after which the oscillations decay and the system stabilizes by 53 ms. The corresponding simulation in Fig. 13b, performed for a loop with stiffness ratio 12.8 at $\tilde{p} = -5$ and $\tilde{\zeta}_\perp = 2$, reproduces these damped oscillatory features. Fig. 13c further quantifies the damping effect by tracking the transverse displacement of the midpoint of the softer segment.

To elucidate the mechanisms underlying the damped oscillations, Fig. 14 shows the temporal evolution of the energy change and dissipation rate at $\tilde{p} = 5$ and -5. The ground bending and surface energies before the soap film rupture are $E_{b0} = 99.8876 B_1/L$ and $E_{t0} = 0.0702\, pL^2$, respectively. Similar to the case of homogeneous rod loops in Fig. 7, the bending energy change $\Delta E_b = E_b - E_{b0}$ and the surface energy change $\Delta E_t = E_t - E_{t0}$ oscillate out of phase with decreasing amplitude. The system evolves slowly and quickly enters a

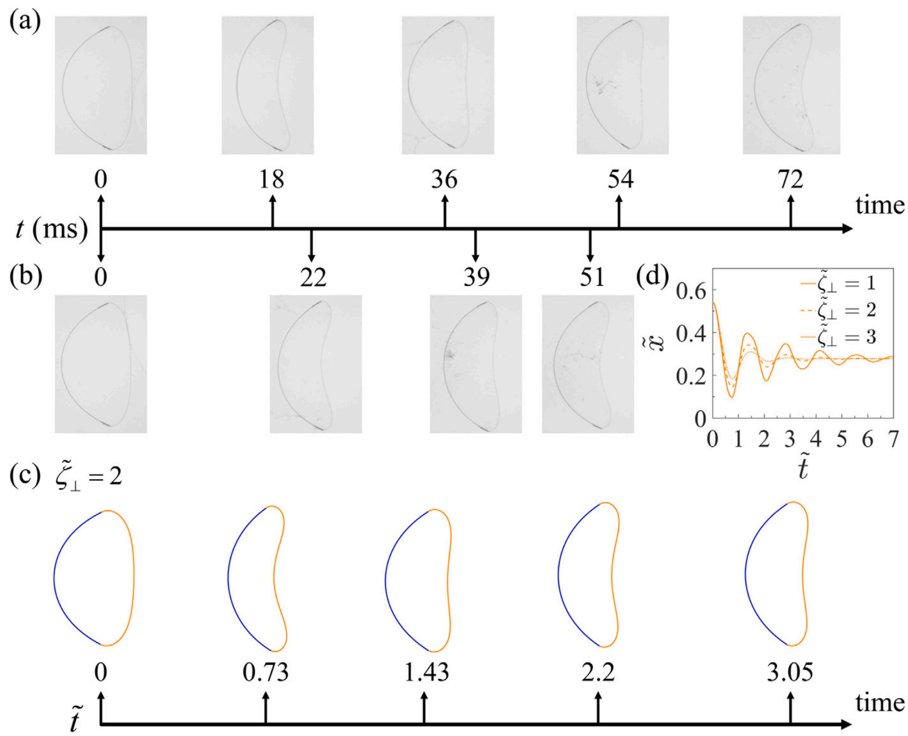

Fig. 12. Oscillatory response of stiffness-inhomogeneous rod loops following outer-film rupture. (a, b) Experimental observations, with (b) showing a case of increased film viscosity achieved using a thickening agent. (c) Simulation of a loop with stiffness ratio $B_2/B_1 = 12.8$ subjected to normalized pressure $\tilde{p} = 5$ and normalized viscous drag $\tilde{\zeta}_\perp = 2$. (d) Time evolution of the transverse displacement $\tilde{x}$ at the midpoint of the softer segment for different $\tilde{\zeta}_\perp = 1$, 2, and 3. The segment junction is located at $\tilde{x} = 0$. In (c), no shift of the simulation time origin is required because the stiffness-inhomogeneous loop exhibits no initial growth stage before visible deformation. Using t of the experimental snapshots in (a) and $\tilde{t}$ of the simulation in (c), $t/\tilde{t}$ is estimated to be approximately 23.6–25.2 ms, in good agreement with the value of about 24 ms predicted by Eq. (8).

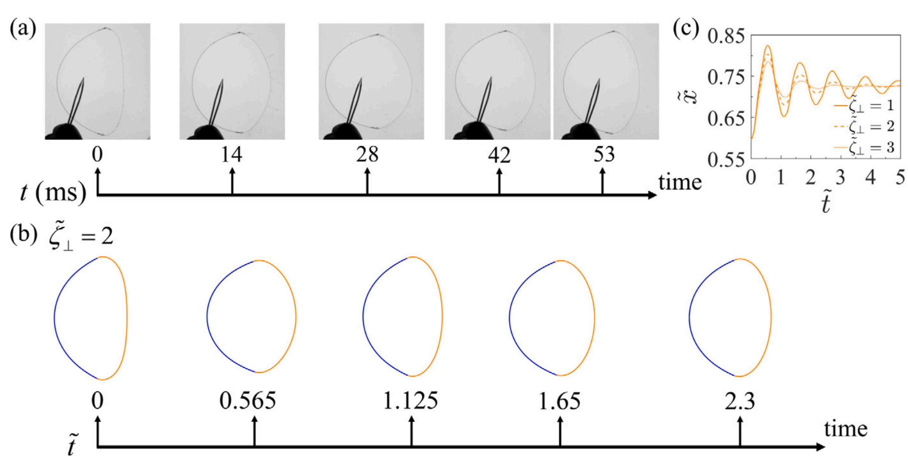

Fig. 13. Oscillatory response of stiffness-inhomogeneous rod loops following inner-film rupture. (a) Experimental observations. (b) Simulation of a loop with stiffness ratio $B_2/B_1 = 12.8$ subjected to normalized pressure $\tilde{p} = -5$ and normalized viscous drag $\tilde{\zeta}_\perp = 2$. (c) Temporal evolution of the transverse displacement $\tilde{x}$ at the midpoint of the softer segment at $\tilde{\zeta}_\perp = 1$, 2, and 3.

quasi-static regime: the kinetic and dissipated energies saturate early, while subsequent changes in bending and tension energies proceed only gradually. Most viscous energy loss is concentrated in the first contraction/expansion–rebound cycle.

A comparison between the outer-film rupture (Figs. 12 and 14a) and inner-film rupture (Figs. 13 and 14b) cases shows that inner-film rupture generates significantly lower deformation amplitudes, which manifest as smaller oscillations in both bending and surface-tension energies. Although the cumulative dissipated energy E_d is also smaller in this case, its fraction of the total energy change is higher. This occurs because inner-film rupture injects a much smaller amount of mechanical energy into the system at the onset: the induced curvature changes are milder, and the subsequent elastic energy excursions are limited. As a result, even modest viscous losses account for a relatively

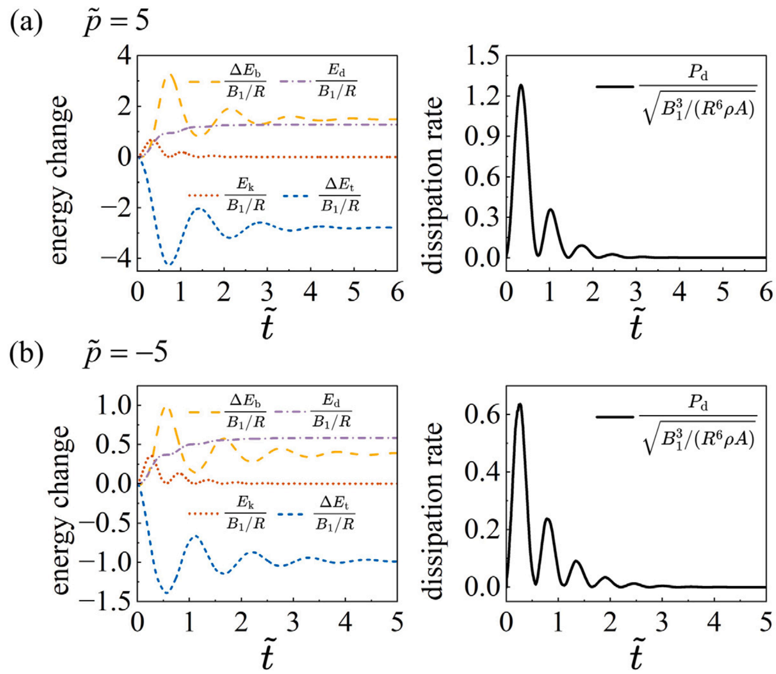

Fig. 14. Temporal evolution of the energy change and dissipation rate for the stiffness-inhomogeneous rod loop ($B_2/B_1 = 12.8$) at normalized pressure $\tilde{p} = 5$ (a) and $\tilde{p} = -5$ (b). The normalized energy components include the bending energy change $\Delta E_b/(B_1/R)$, surface energy change $\Delta E_t/(B_1/R)$, kinetic energy $E_k/(B_1/R)$, and accumulated dissipated energy $E_d/(B_1/R)$, all measured relative to the initial equilibrium configuration taken as the ground state. P_d is the instantaneous dissipation rate. Most viscous energy loss is concentrated in the first contraction/expansion–rebound cycle.

large portion of the total energy budget. In contrast, outer-film rupture delivers an inward impulsive load that drives large-amplitude deformation and substantial elastic energy exchange; the absolute dissipation is higher, but it represents a smaller fraction of the much larger total energy involved.

5.5. Effects of density inhomogeneity on multimodal deformation in the absence of dissipation

To examine how density inhomogeneity alters the undamped oscillatory dynamics, we consider a composite loop consisting of two equal-length segments with the same bending stiffness B but with different densities: the lower-density segment (orange, ρ_1) and the higher-density segment (purple, $\rho_2 > \rho_1$). In the homogeneous case, the number of unstable lobes increases with increasing pressure, and the most unstable mode accurately predicts the initial number of geometric lobes (Eq. (17) and Fig. 2). For the composite loop with piecewise constant density, an analytical dispersion relation is no longer applicable. Instead, the problem reduces to a piecewise eigenvalue formulation: the linearized governing equation is solved separately in each segment, and the resulting solutions are coupled through continuity conditions at the interfaces $s = 0$ and s^*. This leads to a homogeneous linear system for the modal amplitudes of the perturbation, with admissible frequencies determined by the vanishing of the associated determinant. In general, this frequency equation does not admit a closed-form solution and must be solved numerically.

To demonstrate the density effects on the oscillatory dynamics, we first consider the case of $\rho_2 = 5\rho_1$ at a low pressure $\tilde{p} = 3.8$ (Fig. 15). In the undamped case, the time evolution of the loop shapes reveals pronounced dynamic asynchrony between the two segments (Fig. 15a,b). The lower-density (orange) segment responds slightly faster due to the smaller inertia, exhibiting quicker contraction and larger excursions, whereas the higher-density (purple) segment lags, leading to a growing phase mismatch. For example, at $\tilde{t} = 8.5$, the orange segment has already begun to rebound, while the purple segment remains in its first contraction phase.

This desynchronization persists through the subsequent deformation. Shortly after $\tilde{t} = 8.5$, the purple segment briefly pauses, whereas the orange segment continues rebounding, driving a transition of the central region from convex to concave between $\tilde{t} = 10.6$ and 11.5. As oscillations progress, the system enters a complex regime involving alternating contraction–rebound dynamics and asymmetric swaying (e.g., $\tilde{t} = 12.3$, 13.8, and 14.4). At later times $\tilde{t} = 22.7$ and 24.1, the two segments gradually re-synchronize as the phase difference diminishes, with a quasi–time-reversal point observed near $\tilde{t} = 23.4$.

Beyond altering the timing and phasing of the response, the mass mismatch impacts how energy is redistributed within the system. As shown in Fig. 15c, the bending, surface tension, and kinetic energies fluctuate irregularly. These irregular modulations reflect the coexistence of multiple non-harmonically related oscillation frequencies induced by the density contrast.

Fig. 16 further illustrates the effect of density inhomogeneity at higher pressure. The rod loop undergoes stronger acceleration, resulting in faster radial contraction, larger oscillation amplitudes, and the emergence of higher-order undulations. The higher-density segment (purple), due to its greater inertia, deforms less and exhibits smoother curvature evolution. In contrast, the lower-density segment (orange) develops pronounced curvature variations and high-amplitude wavy deformations that localize away from the junction. Consistently, the corresponding force profiles become increasingly irregular and spatially distributed, reflecting the complex interplay between inertia, tension, and density contrast. In contrast to the stiffness-inhomogeneous cases in Fig. 11, no pronounced mode-reduction behavior is observed in Fig. 16.

5.6. Combined effects of stiffness and density inhomogeneities on multimodal deformation in the absence of dissipation

Compared with the stiffness-only results in Section 5.3 and the density-only results in Section 5.5, Fig. 17 shows the multimodal deformation of loops with combined stiffness and density inhomogeneities in the absence of dissipation. The stiffness ratio is fixed at $B_2/B_1 = 2$, while the density ratio in panels (a)–(d) is $\rho_2/\rho_1 = 5$, and in panels

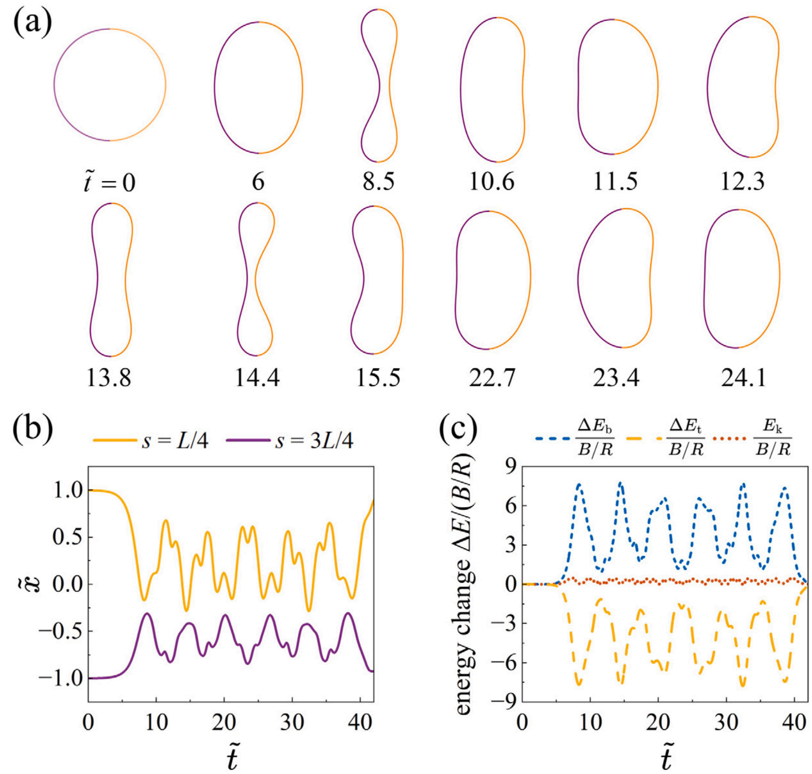

Fig. 15. Post-instability oscillatory response of a density-inhomogeneous rod loop (lower-density segment in orange with density ρ_1, higher-density segment in purple with density ρ_2) at normalized pressure $\tilde{p} = 3.8$ in the absence of viscous dissipation, with density ratio $\rho_2/\rho_1 = 5$. (a) Time evolution of the deformed configurations, illustrating pronounced asynchronous motion between the two segments. (b) Transverse displacement histories $\tilde{x}$ at $s = L/4$ and $3L/4$. (c) Temporal evolution of the normalized energy components, showing irregular fluctuations associated with multiple non-harmonically related oscillation frequencies induced by mass imbalance.

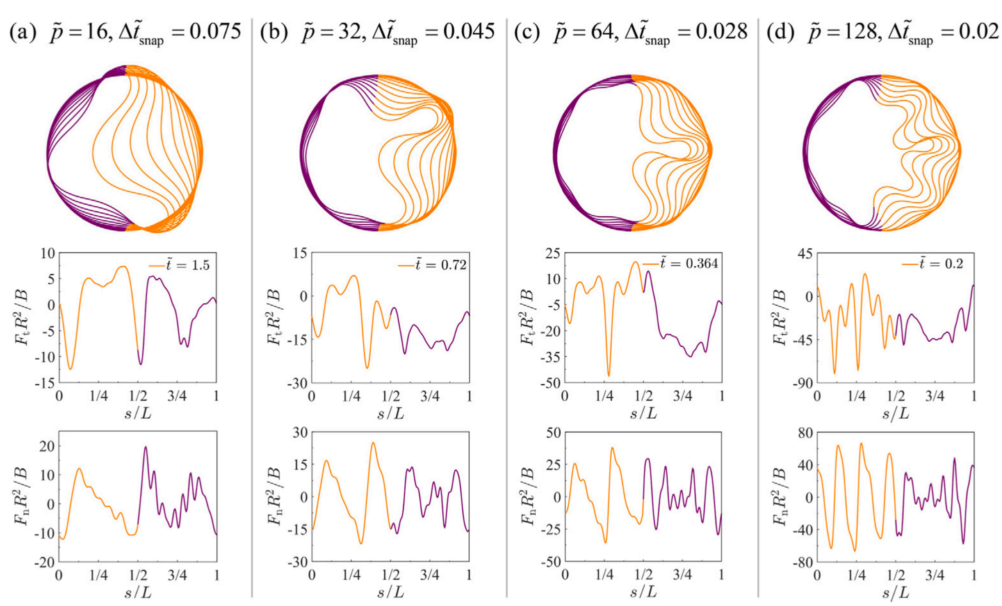

Fig. 16. Snapshots and internal force profiles of a density-inhomogeneous rod loop under pressure $\tilde{p}$. The loop comprises two segments: a lower-density segment (orange) with density ρ_1 and a higher-density segment (purple) with density $\rho_2 = 5\rho_1$. Panels (a)–(d) correspond to $\tilde{p} = 16$, 32, 64, and 128, respectively. The time interval $\Delta\tilde{t}_{snap}$ between successive snapshots is indicated for each case. The total simulation times are 1.5, 0.72, 0.364, and 0.2, respectively. Top row: successive configuration snapshots during the deformation process; the arclength s is defined at the lower segment junction and increases counterclockwise. For each $\tilde{p}$, the middle and the bottom rows show the axial and shear force profiles evaluated at the final simulation time corresponding to the most deformed configuration shown in the top row.

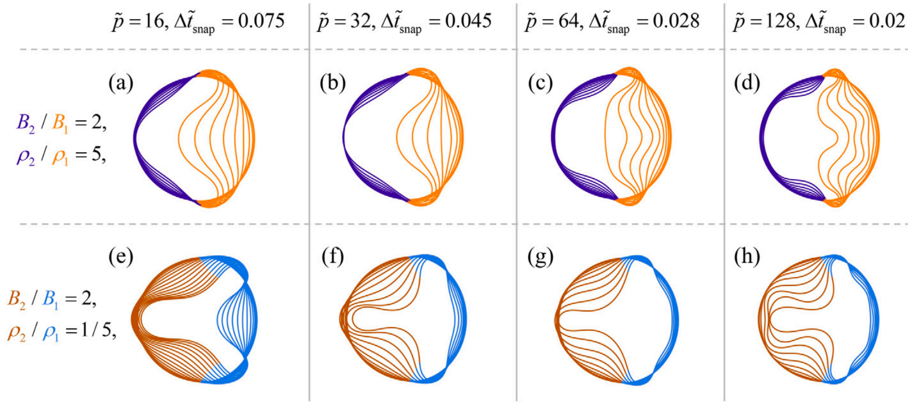

Fig. 17. Multimodal deformation of rod loops with combined stiffness and density inhomogeneities in the absence of dissipation. The loop consists of two equal-length segments with fixed stiffness ratio $B_2/B_1 = 2$. Panels (a)–(d) correspond to $\rho_2/\rho_1 = 5$, where the left segment is both stiffer and heavier; panels (e)–(h) correspond to $\rho_2/\rho_1 = 1/5$, where the left segment is stiffer but lighter. $\tilde{p} = 16$ in (a,e), 32 in (b,f), 64 in (c,g), and 128 in (d,h). Each panel shows successive configuration snapshots during the deformation process, and $\Delta\tilde{t}_{snap}$ denotes the time interval between successive snapshots.

(e)–(h) is $\rho_2/\rho_1 = 1/5$. The stiffness contrast mainly controls the modal character of deformation, with the softer segment developing higher-order undulations, whereas the density contrast mainly affects the inertial response and thus the evolution rate. The lighter segment evolves more rapidly and therefore exhibits a larger extent of deformation. Lobe collapse is observed in the lighter segment in Fig. 17b,c, whereas at higher pressure, lobe coalescence emerges in the lighter segment (Fig. 17d,h).

Finally, we provide three supplementary movies illustrating the post-buckling recovery of homogeneous and inhomogeneous loops at $\tilde{p} = 3.8$ in dissipative systems of $\tilde{\zeta}_\perp = 1$. Movie S1 shows symmetric damped oscillations in a homogeneous loop. Movie S2 demonstrates synchronized but amplitude-asymmetric damping in a stiffness-inhomogeneous loop with $B_2/B_1 = 5$. Movie S3 shows asynchronous damping in a density-inhomogeneous loop with $\rho_2/\rho_1 = 5$.

6. Conclusion

In this work, we combine theoretical and experimental analyses to investigate surface-tension-driven dynamic buckling and oscillations of elastic rod loops. For homogeneous loops, we identify a transition from low-tension oscillatory response to high-tension multimodal buckling. The initially selected lobe number follows the fastest-growing mode from linear stability analysis, whereas the subsequent reduction in lobe number results from nonlinear evolution via lobe coalescence and collapse.

We further show that spatial inhomogeneity fundamentally reshapes the dynamics. Stiffness contrast modifies the instability threshold and deformation distribution, while density contrast alters the inertial response, leading to phase lag, asynchronous motion, and multi-frequency behavior. Their combined effects produce increasingly localized and less synchronized multimodal patterns, while viscous dissipation damps the motion and accelerates relaxation.

Taken together, these results provide a unified picture of how elasticity, inertia, and interfacial dissipation govern dynamic instability and pattern selection in slender structures coupled to deformable interfaces. The underlying mechanisms are expected to extend to a broad class of filament–interface systems undergoing rapid, nonequilibrium deformation, and may inform the design of responsive filamentary structures that exploit controlled instability and damping for shape morphing and energy dissipation.

Looking forward, further progress may be achieved by developing more realistic dissipation models for quantitative experiment–simulation comparison, extending the framework to three-dimensional and out-of-plane instabilities, and generalizing to filament models beyond the inextensible elastica, including extensibility, torsion, and plasticity. These extensions are particularly relevant in regimes involving large deformation, geometric confinement, or rapid loading, where out-of-plane buckling, twist–bend coupling, and irreversible localization can become dominant, further enriching the dynamics of pattern formation.

CRediT authorship contribution statement

Yaxin Fang: Writing – original draft, Validation, Investigation, Formal analysis. **Chengyao Zhang:** Investigation. **Xiying Li:** Investigation. **Yi Man:** Investigation. **Xin Yi:** Writing – review & editing, Supervision, Investigation, Formal analysis, Conceptualization.

Declaration of competing interest

The authors declare that they have no known competing financial interests or personal relationships that could have appeared to influence the work reported in this paper.

Acknowledgments

This work was supported by the National Natural Science Foundation of China under grant 12588301. Computational resources supported by the High-performance Computing Platform of Peking University are acknowledged.

Appendix A. Rotational inertia moment

We estimate the scales of each term in the angular momentum balance in Eq. (1). Let R be the characteristic length scale (e.g., the effective rod loop radius) and T_0 a characteristic time scale of the motion. Then $\mathbf{t}\times\mathbf{F}\sim\mathbf{F}\sim\partial\mathbf{M}/\partial s\sim B/R^2$ and $\rho I\mathbf{n}\times(\partial^2\mathbf{n}/\partial t^2)\sim\rho I/T_0^2$. Since $\rho A(\partial^2\mathbf{r}/\partial t^2)\sim\rho AR/T_0^2$ and $\partial\mathbf{F}/\partial s\sim B/R^3$, the linear momentum balance in Eq. (1) gives $\rho AR/T_0^2\sim B/R^3$ or $1/T_0^2\sim B/(\rho AR^4)$. Then the rotational inertia term $\rho I\mathbf{n}\times(\partial^2\mathbf{n}/\partial t^2)$ scales as $\rho I\mathbf{n}\times(\partial^2\mathbf{n}/\partial t^2)\sim BI/(AR^4)$. Comparison with $\partial\mathbf{M}/\partial s\sim B/R^2$ gives the ratio

$$\frac{\rho I\mathbf{n}\times(\partial^2\mathbf{n}/\partial t^2)}{\partial\mathbf{M}/\partial s}\sim\frac{I}{AR^2}\sim\left(\frac{a}{R}\right)^2. \tag{A.1}$$

where a is the cross-section radius of thin rods.

Eq. (A.1) shows that, for slender rods with $(a/R)^2\ll 1$, the rotational inertia term $\rho I\mathbf{n}\times(\partial^2\mathbf{n}/\partial t^2)$ is negligible compared with $\partial\mathbf{M}/\partial s$. In our experiments, the rod loops have $a\approx 0.1$ mm and $R\approx 4.5$ cm, giving $(a/R)^2=\mathcal{O}(10^{-6})$. This small parameter justifies neglecting the rotational inertia term in both the theoretical formulation and the experimental regime considered.

Appendix B. Discretization scheme

To solve Eqs. (10)–(13), a finite difference method is employed. A central-difference scheme is used for the spatial derivatives along the arclength s, while a backward-difference scheme is adopted for the time discretization. The rod loop is uniformly discretized into N grid points, separated by a spacing $\Delta s = L/N$ or $\Delta\tilde{s} = 2\pi/N$. When the surface tension is large, the loop may exhibit complex dynamic buckling, requiring a large N (e.g., $N = 300$) to accurately capture its shape evolution. To ensure numerical stability, a small time step $\Delta\tilde{t}$ (e.g., $\Delta\tilde{t} = 10^{-3}$) is used.

Within the discretized domain, each grid point is labeled by the spatial index i, and the associated variables at time step $j(\geq 1)$ are denoted as $\tilde{\boldsymbol{q}}_i^j = \{\tilde{x}_i^j, \tilde{y}_i^j, \theta_i^j, \tilde{\kappa}_i^j, \tilde{F}_{x,i}^j, \tilde{F}_{y,i}^j\}$. The midpoint between two neighboring points i and $i+1$ satisfies the discrete averaging condition $\tilde{\boldsymbol{q}}_{i+1/2}^j = (\tilde{\boldsymbol{q}}_i^j + \tilde{\boldsymbol{q}}_{i+1}^j)/2$, and the corresponding arclength derivative is approximated by $\mathrm{d}(\tilde{\boldsymbol{q}}_{i+1/2}^j)/\mathrm{d}s = (\tilde{\boldsymbol{q}}_{i+1}^j - \tilde{\boldsymbol{q}}_i^j)/\Delta\tilde{s}$.

At the first time step ($j = 1$), the equilibrium configuration at $p = 0$ is used as the initial shape, circular for a homogeneous loop and energy-minimized for an inhomogeneous loop. Small radial perturbations of magnitude $\epsilon(\ll R)$ are introduced to the initially circular loop to trigger symmetry breaking and subsequent dynamic evolution.

From the second time step onward, a backward-difference scheme is applied for the temporal derivatives. For example, the velocity at the midpoint $i + 1/2$ for the second time step ($j = 2$) is calculated as

$$\tilde{v}_{x,i+1/2}^2 = \frac{(\tilde{x}_{i+1}^2 - \tilde{x}_{i+1}^1) + (\tilde{x}_i^2 - \tilde{x}_i^1)}{2\,\Delta\tilde{t}}. \tag{B.1}$$

With the zero initial velocity condition $\tilde{v}_{x,i+1/2}^1 = 0$, the acceleration at $j = 2$ becomes

$$\tilde{a}_{x,i+1/2}^2 = \frac{\tilde{v}_{x,i+1/2}^2 - \tilde{v}_{x,i+1/2}^1}{\Delta\tilde{t}} = \frac{\tilde{v}_{x,i+1/2}^2}{\Delta\tilde{t}}. \tag{B.2}$$

Once the positions and velocities at the first two steps are known, subsequent values are updated recursively using the second-order backward-difference scheme as

$$\begin{aligned} &\tilde{v}_{x,i}^j = \frac{3\tilde{x}_i^j - 4\tilde{x}_i^{j-1} + \tilde{x}_i^{j-2}}{2\Delta\tilde{t}}, \quad \tilde{v}_{x,i+1/2}^j = \frac{\tilde{v}_{x,i}^j + \tilde{v}_{x,i+1}^j}{2}, \\ &\tilde{a}_{x,i+1/2}^j = \frac{3\tilde{v}_{x,i+1/2}^j - 4\tilde{v}_{x,i+1/2}^{j-1} + \tilde{v}_{x,i+1/2}^{j-2}}{2\Delta\tilde{t}} \quad (j \geq 3). \end{aligned} \tag{B.3}$$

The same procedure is applied to the y-components of velocity (v_y) and acceleration (a_y), i.e., by directly replacing x with y in the above finite-difference expressions.

Based on the discretization schemes described above, the complete finite-difference representations of Eqs. (10)–(13) with $j \geq 3$ can be written as

$$\begin{cases} \dfrac{\tilde{x}_{i+1}^j - \tilde{x}_i^j}{\Delta\tilde{s}} = \cos\theta_{i+1/2}^j, \quad \dfrac{\tilde{y}_{i+1}^j - \tilde{y}_i^j}{\Delta\tilde{s}} = \sin\theta_{i+1/2}^j, \\ \dfrac{\tilde{F}_{x,i+1}^j - \tilde{F}_{x,i}^j}{\Delta\tilde{s}} - \tilde{p}\sin\theta_{i+1/2}^j - \tilde{\zeta}_\perp\Big[(\gamma\cos^2\theta_{i+1/2}^j + \sin^2\theta_{i+1/2}^j)\tilde{v}_{x,i+1/2}^j \\ \quad + (\gamma-1)\sin\theta_{i+1/2}^j\cos\theta_{i+1/2}^j\tilde{v}_{y,i+1/2}^j\Big] = \tilde{\rho}_{i+1/2}^j\tilde{a}_{x,i+1/2}^j, \\ \dfrac{\tilde{F}_{y,i+1}^j - \tilde{F}_{y,i}^j}{\Delta\tilde{s}} + \tilde{p}\cos\theta_{i+1/2}^j - \tilde{\zeta}_\perp\Big[(\gamma-1)\sin\theta_{i+1/2}^j\cos\theta_{i+1/2}^j\tilde{v}_{x,i+1/2}^j \\ \quad + (\gamma\sin^2\theta_{i+1/2}^j + \cos^2\theta_{i+1/2}^j)\tilde{v}_{y,i+1/2}^j\Big] = \tilde{\rho}_{i+1/2}^j\tilde{a}_{y,i+1/2}^j, \\ \dfrac{\tilde{B}_{i+1}^j\tilde{\kappa}_{i+1}^j - \tilde{B}_i^j\tilde{\kappa}_i^j}{\Delta\tilde{s}} - \tilde{F}_{x,i+1/2}^j\sin\theta_{i+1/2}^j + \tilde{F}_{y,i+1/2}^j\cos\theta_{i+1/2}^j = 0 \\ \text{with} \quad \tilde{\kappa}_{i+1/2}^j = \dfrac{\theta_{i+1}^j - \theta_i^j}{\Delta\tilde{s}}. \end{cases} \tag{B.4}$$

Appendix C. Mode coalescence and collapse under high pressure and the effect of initial perturbation amplitude

To clarify the relation between the linear stability prediction and the subsequent nonlinear evolution, and to assess the influence of the initial perturbation amplitude, additional simulations are performed at a relatively high pressure $\tilde{p} = 64$ (Fig. C.1).

Two perturbation amplitudes are considered: a smaller amplitude $\epsilon = 5\times10^{-5}R$ (Fig. C.1a–d; corresponding to Fig. 5c) and a larger one $\epsilon = 5\times10^{-3}R$ (Fig. C.1e–h). In both cases, the initial buckling pattern is a six-lobed shape, consistent with the most unstable mode predicted by Eq. (17) and Fig. 2. As the nonlinear evolution proceeds, neighboring lobes merge or individual lobes collapse, leading to a reduction in the mode number, from $n = 6$ to 5 and, in some cases, further to 4.

Comparing the temporal evolution of the loop configurations shows that a smaller perturbation delays the emergence of clearly developed lobes, but leads to a more regular buckling pattern at early times.

To elucidate the mechanism underlying the mode reduction, we examine the speed distribution along the loop, with configurations color-coded by the local speed magnitude $\tilde{v} = \sqrt{\tilde{v}_x^2 + \tilde{v}_y^2}$ (Fig. C.1). The reduction in mode number proceeds through two representative pathways: lobe coalescence and lobe collapse. In the lobe coalescence pathway, the valley between two neighboring lobes, which is characterized by relatively low curvature and slow motion, is progressively smoothed out, leading to the merging of the two lobes (Fig. C.1a, $n = 6$ to 5 and Fig. C.1e, $n = 5$ to 4). In the lobe collapse pathway, within a local three-lobe structure, the middle lobe moves inward faster than its neighbors, leading to a gradual transformation from a convex protrusion into a concave indentation, resulting in a transition from three lobes to two (Fig. C.1e, $n = 6$ to 5). Both pathways lead to a reduction in the mode number.

The mode reduction is also reflected in the curvature profiles (Fig. C.1b–d and f–h). For the lobe coalescence, a region initially characterized by two curvature peaks separated by a valley evolves as the peaks decrease and the valley rises, eventually forming a single peak (orange boxed frames in Fig. C.1b and f). For the lobe collapse, the curvature in the affected region changes sign, corresponding to the transformation from a convex lobe to a concave indentation. These observations confirm that the reduction in mode number is a nonlinear process driven by spatially non-uniform local motion.

Appendix D. Numerical method for calculating the critical buckling pressure

The critical pressure for the static buckling is computed using a constrained energy minimization approach under area conservation. The loop configuration is parameterized by a truncated Fourier representation of the tangent angle [80]

$$\theta(\tilde{s}) = \frac{2\pi s}{L} + \sum_{m=1}^{M} a_m \sin\frac{\pi m s}{L} = \tilde{s} + \sum_{m=1}^{M} a_m \sin\frac{m\tilde{s}}{2}, \tag{D.1}$$

where $L = 2\pi R$ is the rod length, M is the number of Fourier modes, and a_m denote the Fourier coefficients. The loop closure is enforced by requiring periodicity of the centerline, i.e., continuity of both x- and y-coordinates at $\tilde{s} = 0$ and 2π, enforced by $\oint\cos\theta\,\mathrm{d}\tilde{s} = 0$ and $\oint\sin\theta\,\mathrm{d}\tilde{s} = 0$.

At $p = 0$, the equilibrium configuration and its enclosed area A_0 are obtained by minimizing the bending energy E_b subject to fixed rod length L and loop-closure constraints, using a sequential quadratic programming algorithm. To determine the critical pressure, we then impose a slightly reduced enclosed area $A_\mathrm{enclosed} = \alpha A_0$ ($\alpha < 1$), and solve the constrained minimization problem again. The Lagrange multiplier associated with the area constraint is identified as the effective pressure $p(\alpha)$, and the critical pressure is obtained in the limit $p_\mathrm{cr} = \lim_{\alpha\to1} p(\alpha)$.

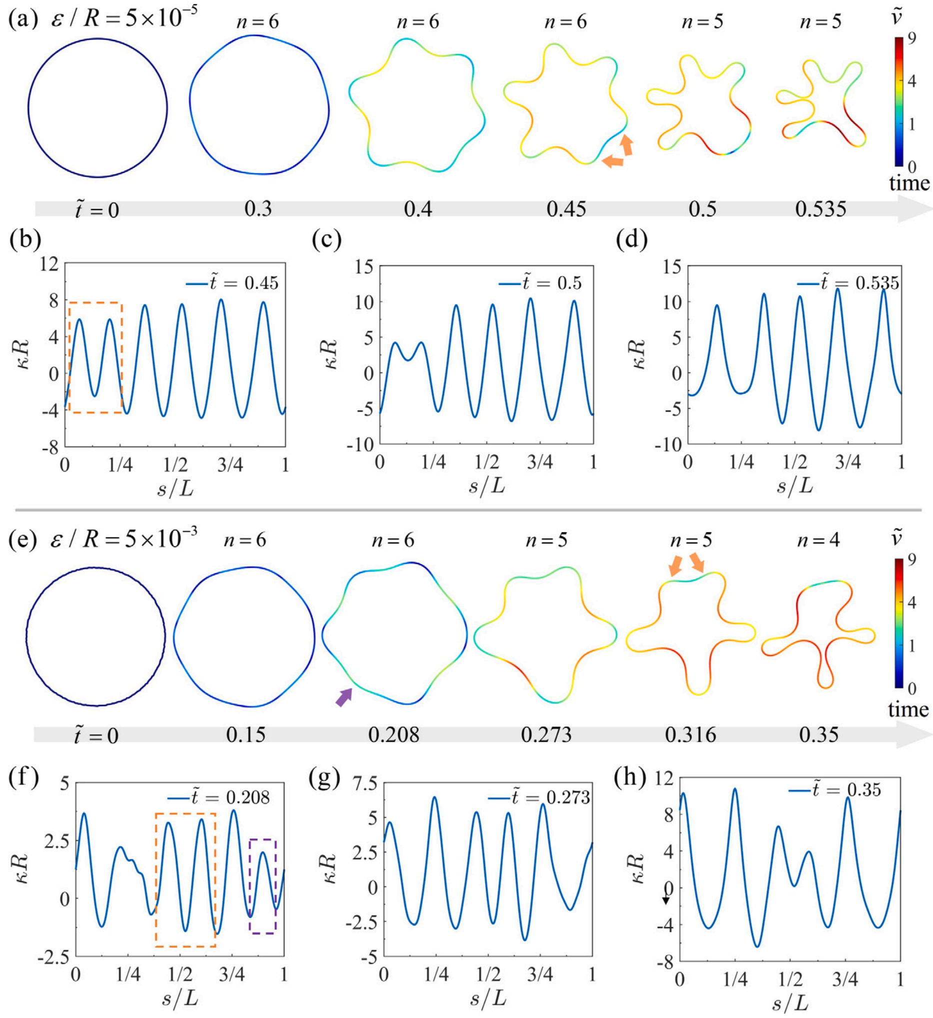

Fig. C.1. Temporal evolution of the loop configurations, speed distributions, and curvature profiles for the homogeneous elastic rod loop at $\tilde{p} = 64$. Two radial perturbation amplitudes are imposed: $\varepsilon/R = 5\times10^{-5}$ (a–d) and 5×10^{-3} (e–h). Panels (a) and (e) show successive loop configurations color-coded by the local speed magnitude $\tilde{v} = \sqrt{\tilde{v}_x^2 + \tilde{v}_y^2}$. Panels (b–d) and (f–h) show the corresponding curvature profiles at selected times from (a) and (e), respectively. Arrows indicate regions of lobe coalescence and lobe collapse, both contributing to the reduction of the mode number.

To validate the numerical procedure, we apply this method to a homogeneous rod loop with the known result $\tilde{p}_{cr} = 3$. The calculated normalized effective pressure $\tilde{p}(\alpha) = p(\alpha)R^3/B_1$ converges rapidly to this value as $\alpha \to 1$, yielding 3.087, 3.016, 3.0016, and 3.0001 for $\alpha =$ 0.95, 0.99, 0.999, and 0.9999, respectively. This robust convergence justifies the choice $\alpha = 0.9999$ in the present calculations.

Appendix E. Supplementary data

Supplementary material related to this article can be found online at https://doi.org/10.1016/j.ijmecsci.2026.111841.

Data availability

Data will be made available on request.

References

[1] Fraldi M, Guarracino F. Towards an accurate assessment of UOE pipes under external pressure: effects of geometric imperfection and material inhomogeneity. Thin-Walled Struct 2013;63:147–62.

[2] Godoy LA. Buckling of vertical oil storage steel tanks: Review of static buckling studies. Thin-Walled Struct 2016;103:1–21.

[3] Foster B, Verschueren N, Knobloch E, Gordillo L. Universal wrinkling of supported elastic rings. Phys Rev Lett 2022;129:164301.

[4] Rubinow SI, Keller JB. Flow of a viscous fluid through an elastic tube with applications to blood flow. J Theor Biol 1972;35:299–313.

[5] Moulton DE, Goriely A. Circumferential buckling instability of a growing cylindrical tube. J Mech Phys Solids 2011;59:525–37.

[6] Feng X-Q, Li B, Lin SZ, Wang MY, Chen XD, Zhang HX, Fang W. Mechano-chemo-biological theory of cells and tissues: Review and perspectives. Acta Mech Sin 2025;41:625315.

[7] Lu L, Leanza S, Zhao RR. Mechanical instabilities: From failure mechanism to functionality. Appl Mech Rev 2026;78:030801.

[8] Pontin M, Damian DD. Multimodal soft valve enables physical responsiveness for preemptive resilience of soft robots. Sci Robot 2024;9:eadk9978.

[9] Lee W-K, Preston DJ, Nemitz MP, Nagarkar A, MacKeith AK, Gorissen B, Vasios N, Sanchez V, Bertoldi K, Mahadevan L, Whitesides GM. A buckling-sheet ring oscillator for electronics-free, multimodal locomotion. Sci Robot 2022;7:eabg5812.

[10] Pancaldi L, Özelçi E, Gadiri MA, Raub J, Mosimann PJ, Sakar MS. Flow-driven magnetic microcatheter for superselective arterial embolization. Sci Robot 2025;10:eadu4003.

[11] Chen G, Long Y, Yao S, Tang S, Luo J, Wang H, Zhang Z, Jiang H. A non-electrical pneumatic hybrid oscillator for high-frequency multimodal robotic locomotion. Nat Commun 2025;16:1449.

[12] Park J-S, Ki K, Lee A, Sun J-Y, Kim H-Y. Snap inflatable modular metastructures for multipath, multimode morphing machines. Cell Rep Phys Sci 2025;6:102448.

[13] Wu C, Liu H, Lin S, Lam J, Xi N, Chen Y. Shape morphing of soft robotics by pneumatic torsion strip braiding. Nat Commun 2025;16:3787.

[14] Lévy M. Mémoire sur un nouveau cas intégrable du problème de l'élastique et l'une de ses applications. J Math Pures Appl 1884;10:5–42.
[15] Antman S, Warner WH. Dynamic stability of circular rods. J Soc Ind Appl Math 1965;13:1007–18.
[16] Flaherty JE, Keller JB. Contact problems involving a buckled elastica. SIAM J Appl Math 1973;24:215–25.
[17] Carrier GF. On the buckling of elastic rings. J Math Phys 1947;26:94–103.
[18] Boresi AP. A refinement of the theory of buckling of rings under uniform pressure. J Appl Mech 1955;22:95–102.
[19] Tadjbakhsh I, Odeh F. Equilibrium states of elastic rings. J Math Anal Appl 1967;18:59–74.
[20] Djondjorov PA, Vassilev VM, Mladenov IM. Analytic description and explicit parametrisation of the equilibrium shapes of elastic rings and tubes under uniform hydrostatic pressure. Int J Mech Sci 2011;53:355–64.
[21] Kumar A, Das SL, Wahi P. Instabilities of thin circular cylindrical shells under radial loading. Int J Mech Sci 2015;104:174–89.
[22] Azzuni E, Guzey S. A perturbation approach on buckling and postbuckling of circular rings under nonuniform loads. Int J Mech Sci 2018;137:86–95.
[23] Mascolo I, Guarracino F. Revisitation of elastic buckling of circular rings: some analytical and numerical issues. Thin-Walled Struct 2023;182:110287.
[24] Guarracino F, Mascolo I. On the inextensibility assumption in the stability of elastic rings: Overhaul of a traditional paradigm. J Appl Mech 2026;93:031002.
[25] Gaibotti M, Bigoni D, Cutolo A, Fraldi M, Piccolroaz A. Effects of different loading on the bifurcation of annular elastic rods: Theory vs. experiments. Int J Non Linear Mech 2024;165:104820.
[26] Vassilev VM, Djondjorov PA, Mladenov IM. Cylindrical equilibrium shapes of fluid membranes. J Phys A Math Theor 2008;41:435201.
[27] Giomi L, Mahadevan L. Minimal surfaces bounded by elastic lines. Proc R Soc A 2012;468:1851–64.
[28] Giusteri GG, Franceschini P, Fried E. Instability paths in the Kirchhoff–Plateau problem. J Nonlinear Sci 2016;26:1097–132.
[29] Palmer B, Pámpano Á. Minimal surfaces with elastic and partially elastic boundary. Proc R Soc Edinb Sect A Math 2021;151:1225–46.
[30] Palmer B, Pámpano Á. Symmetry breaking bifurcation of membranes with boundary. Nonlinear Anal 2024;238:113393.
[31] Tiwari S, Fried E. The out-of-plane bifurcation and narrow stability interval of planar solutions in the Euler–Plateau problem. J Mech Phys Solids 2026;214:106657.
[32] Zhang C, Yi X. Euler-Helfrich problem for open vesicles bounded by elastic filaments. Phys Rev Res 2026;8:013225.
[33] Palmer B, Pámpano Á. Stability of membranes. J Geom Anal 2024;34:328.
[34] Flaherty JE, Keller JB, Rubinow SI. Post buckling behavior of elastic tubes and rings with opposite sides in contact. SIAM J Appl Math 1972;23:446–55.
[35] Napoli G, Goriely A. A tale of two nested elastic rings. Proc R Soc A 2017;473:20170340.
[36] Hazel AL, Mullin T. On the buckling of elastic rings by external confinement. Philos Trans R Soc A 2017;375:20160227.
[37] Lombardo F, Goriely A, Napoli G. Asymmetric equilibria of two nested elastic rings. Mech Res Commun 2018;94:91–4.
[38] Yang P, Dang F, Liao X, Chen X. Buckling morphology of an elastic ring confined in an annular channel. Soft Matter 2019;15:5443–8.
[39] Shi C, Zou G, Wu Z, Wang M, Zhang X, Gao H, Yi X. Morphological transformations of vesicles with confined flexible filaments. Proc Natl Acad Sci USA 2023;120:e2300380120.
[40] Cutolo A, Fraldi M, Napoli G, Puglisi G. Growth of a flexible fibre in a deformable ring. Soft Matter 2023;19:3366–76.
[41] Wang M, Li X, Yi X. Deformation, shape transformations, and stability of elastic rod loops within spherical confinement. J Mech Phys Solids 2024;191:105771.
[42] Alber DS, Zhao S, Jacinto AO, Wieschaus EF, Shvartsman SY, Haas PA. A model for boundary-driven tissue morphogenesis. Proc Natl Acad Sci USA 2025;122:e2505160122.
[43] Shi C, Zhang C, Fang Y, Yi X. Flexible filaments in vesicles with reduced volume: anisotropic confinement and morphological response. J Mech Phys Solids 2026;206:106383.
[44] Zhang C, Zou G, Fang Y, Gao H, Yi X. Interacting filaments drive vesicle morphogenesis. Nat Commun 2026;17:78.
[45] Yan Z, Wang K, Wang B. Buckling of circular rings and its applications in thin-film electronics. Int J Mech Sci 2022;228:107477.
[46] Jin T, Zhao J, Zhang Y. Postbuckling analyses of ribbon-type 3D structures assembled on cylindrical substrates. Acta Mech Sin 2024;40:424130.
[47] Liu T, Zhang G, Du F, Zhang X, He C, Li Y, Song R. Magnetic continuum robot: Design, modeling and verification. Int J Mech Sci 2025;301:110460.
[48] Nelson FC. In-plane vibration of a simply supported circular ring segment. Int J Mech Sci 1962;4:517–27.
[49] Wang G, Qu Y, Li Y. Nonlinear vibration and acoustic radiation of an internally resonant buckled beam. Int J Mech Sci 2024;276:109365.
[50] Xu J, Zhang Y, Negahban M, Wang W, Li Z. Piezoelectric metamaterial curved beams with feedback control for manipulating bandgaps. Int J Mech Sci 2026;311:111175.
[51] Shi H, Wang H, Zhao Z, Liu X, Wei Y. Nonlinear vibrations of a cracked circular ring subjected to moving contact loads. Int J Mech Sci 2026;309:111053.
[52] Wah T. Dynamic buckling of thin circular rings. Int J Mech Sci 1970;12:143–55.
[53] Han J-B, Tvergaard V. Effect of inertia on the necking behaviour of ring specimens under rapid axial expansion. Eur J Mech A Solids 1995;14:287–307.
[54] Zhang H, Ravi-Chandar K. On the dynamics of necking and fragmentation–II. Effect of material properties, geometrical constraints and absolute size. Int J Fract 2008;150:3–36.
[55] Putelat T, Triantafyllidis N. Dynamic stability of externally pressurized elastic rings subjected to high rates of loading. Int J Solids Struct 2014;51:1–12.
[56] Marvi-Mashhadi M, Rodríguez-Martínez JA. Multiple necking patterns in elasto-plastic rings subjected to rapid radial expansion: the effect of random distributions of geometric imperfections. Int J Impact Eng 2020;144:103661.
[57] Chen Z, Liu Y, Sung HJ. Flow-induced oscillations of a clamped flexible ring. J Fluid Mech 2025;1013:A6.
[58] Zhou C, Sui G, Chen Y, Shan X. A nonlinear low frequency quasi zero stiffness vibration isolator using double-arc flexible beams. Int J Mech Sci 2024;276:109378.
[59] Box F, Kodio O, O'Kiely D, Cantelli V, Goriely A, Vella D. Dynamic buckling of an elastic ring in a soap film. Phys Rev Lett 2020;124:198003.
[60] Kodio O, Goriely A, Vella D. Dynamic buckling of an inextensible elastic ring: linear and nonlinear analyses. Phys Rev E 2020;101:053002.
[61] Moffatt HK, Goldstein RE, Pesci AI. Soap-film dynamics and topological transitions under continuous deformation. Phys Rev Fluids 2016;1:060503.
[62] Son K, Guasto JS, Stocker R. Bacteria can exploit a flagellar buckling instability to change direction. Nat Phys 2013;9:494–8.
[63] Lu M, Deng J, Mao X, Brandt L. Dynamic buckling of a filament impacted by a falling droplet. Phys Rev Lett 2023;131:184002.
[64] Larson NM, Mueller J, Chortos A, Davidson ZS, Clarke DR, Lewis JA. Rotational multimaterial printing of filaments with subvoxel control. Nature 2023;613:682–8.
[65] Nguyen T, Manikantan H. Flow-induced buckling of elastic microfilaments with non-uniform bending stiffness. Front Soft Matter 2023;2:977729.
[66] Landau LD, Lifshitz EM. Theory of Elasticity. 3rd ed. New York: Butterworth-Heinemann; 1986.
[67] Cox RG. The motion of long slender bodies in a viscous fluid. Part 1. General theory. J Fluid Mech 1970;44:791–810.
[68] Lauga E, Powers TR. The hydrodynamics of swimming microorganisms. Rep Progr Phys 2009;72:096601.
[69] Man Y, Ling F, Kanso E. Cilia oscillations. Philos Trans R Soc B 2020;375:20190157.
[70] Shi W, Moradi M, Nazockdast E. Hydrodynamics of a single filament moving in a spherical membrane. Phys Rev Fluids 2022;7:084004.
[71] Kadoya K, Matsunaga N, Nagashima A. Viscosity and thermal conductivity of dry air in the gaseous phase. J Phys Chem Ref Data 1985;14:947–70.
[72] Habibi HK, Krechetnikov R. Soap film catastrophes. J Fluid Mech 2021;926:A19.
[73] Saffman PG, Delbrück M. Brownian motion in biological membranes. Proc Natl Acad Sci USA 1975;72:3111–3.
[74] Levine AJ, Liverpool TB, MacKintosh FC. Dynamics of rigid and flexible extended bodies in viscous films and membranes. Phys Rev Lett 2004;93:038102.
[75] Fischer TM. The drag on needles moving in a Langmuir monolayer. J Fluid Mech 2004;498:123–37.
[76] Pandey A, Moulton DE, Vella D, Holmes DP. Dynamics of snapping beams and jumping poppers. EPL 2014;105:24001.
[77] Chopin J, Dasgupta M, Kudrolli A. Dynamic wrinkling and strengthening of an elastic filament in a viscous fluid. Phys Rev Lett 2017;119:088001.
[78] Villermaux E, Keremidis K, Vandenberghe N, Abdolhosseini Qomi MJ, Ulm F-J. Mode coarsening or fracture: Energy transfer mechanisms in dynamic buckling of rods. Phys Rev Lett 2021;126:045501.
[79] Lu M, Mao X, Brandt L, Deng J. Droplet detachment from a vertical filament with one end clamped. Phys Rev Res 2024;6:043003.
[80] Yi X, Gao H. Phase diagrams and morphological evolution in wrapping of rod-shaped elastic nanoparticles by cell membrane: A two-dimensional study. Phys Rev E 2014;89:062712.